JGR Atmospheres

RESEARCH ARTICLE
10.1029/2025JD045130

Revisiting Intrinsic Predictability of Wave-Convection Coupled Bands Over Southern China: Variable and Scale-Dependent Error Growth Characteristics

Manshi Weng[1,2,3], Junhong Wei[1,2,3], Yu Du[1,2,3], Y. Qiang Sun[4], and Xubin Zhang[5]

[1]School of Atmospheric Sciences, Sun Yat-sen University, and Southern Marine Science and Engineering Guangdong Laboratory (Zhuhai), Zhuhai, China, [2]Guangdong Province Key Laboratory for Climate Change and Natural Disaster Studies, Sun Yat-sen University, Zhuhai, China, [3]Key Laboratory of Tropical Atmosphere-Ocean System, Sun Yat-sen University, Ministry of Education, Zhuhai, China, [4]Department of the Geophysical Sciences, University of Chicago, Chicago, IL, USA, [5]Guangzhou Institute of Tropical and Marine Meteorology, China Meteorological Administration, Guangzhou, China

Abstract This study investigates the variable- and scale-dependent intrinsic predictability of wave-convection coupled bands over southern China on 30 January 2018, using 1-km simulations under varying initial moisture conditions. The predictability time is quantified via the Loss Predictability Index (LPI), defined as the ratio of the forecast error power spectrum to the reference (unperturbed) power spectrum at a given scale. Spectral analysis reveals substantial differences in the reference power spectral slopes among variables, while their error growth behaviors consistently exhibit upscale features. The intrinsic predictability limit of the banded convection, measured by the difference total energy (DTE), is approximately 7 hr. Predictability varies with both scale and altitude: smaller scales (i.e., ∼10 km) have shorter limits than larger scales (i.e., ∼40 km), and the middle-level moist neutral stability layer is less predictable than the low-level ducting stable layer. In particular, for the moist neutral stability layer, different variables become more correlated under the coupling between gravity waves and moist convection, yielding more coherent predictability characteristics. In the dry experiment, predictability exceeds 12 hr with minimal error growth, regardless of the variable, scale, or altitude. Finally, the decomposition of the horizontal kinetic energy spectrum into divergent and rotational components demonstrates contrasting power spectra, intrinsic predictability limits, and their sensitivity to initial moist content, with the divergent component exhibiting longer predictability in the ducting stable layer at wavelengths <40 km. These findings highlight how vertical flow structure, moisture content, and distinct dynamical components jointly constrain the intrinsic predictability of mesoscale convective systems.

Plain Language Summary Intrinsic predictability of the weather defines the ultimate limit of our day-to-day weather forecasts, that is, how long forecasts can remain useful before error growth reaches a threshold. This work utilizes very detailed (1 km) computer simulations to investigate the intrinsic predictability of a banded storm system that formed over southern China on 30 January 2018. The results show that this event is predictable for less than ∼7 hr, in general. Additionally, small features (about 10 km across) lose accuracy faster than larger ones (about 40 km), and storms in mid-level moist layers are harder to predict than those in low-level stable layers. However, in dry conditions, forecasts stay accurate for more than 12 hr. It is also found that different types of wind motion and other meteorological factors lose predictability at different rates. Overall, these results reveal what limits forecasts of intense, organized storms.

Key Points:

- Mesoscale intrinsic predictability exhibits a distinct vertical contrast, as it is significantly lower in the mid-level moist neutral layer
- Moisture catalyzes rapid error growth and establishes more coherent predictability features among variables
- At scales <40 km, the divergent flow exhibits less moisture sensitivity and higher intrinsic predictability than the rotational flow

Supporting Information:

Supporting Information may be found in the online version of this article.

Correspondence to:

J. Wei,
weijunh@mail.sysu.edu.cn

Citation:

Weng, M., Wei, J., Du, Y., Sun, Y. Q., & Zhang, X. (2026). Revisiting intrinsic predictability of wave-convection coupled bands over southern China: Variable and scale-dependent error growth characteristics. *Journal of Geophysical Research: Atmospheres*, *131*, e2025JD045130. https://doi.org/10.1029/2025JD045130

Received 27 AUG 2025
Accepted 4 APR 2026

Author Contributions:

Conceptualization: Junhong Wei
Formal analysis: Manshi Weng, Junhong Wei
Investigation: Manshi Weng
Methodology: Manshi Weng, Junhong Wei, Y. Qiang Sun
Resources: Yu Du
Supervision: Junhong Wei
Visualization: Manshi Weng
Writing – original draft: Manshi Weng
Writing – review & editing: Junhong Wei, Yu Du, Y. Qiang Sun, Xubin Zhang

1. Introduction

Atmospheric predictability research is one of the most fundamental scientific issues in addressing the practical applications of numerical weather prediction (NWP) models. It is of paramount significance to understand the uncertainties in forecasts, to investigate the predictability limit of day-to-day weather phenomena in theory, and to explore how to better improve deterministic predictions in practice (Min & Wu, 2020; Mu et al., 2017). In general, the concept of atmospheric predictability can be categorized into two types (Lorenz, 1996; Melhauser & Zhang, 2012): (a) Practical predictability refers to the actual forecasting capability of the atmosphere based on the initial conditions generated by current optimal analysis methods and forecasting models (Lorenz, 1982). It is closely related to both forecast model uncertainties and initial condition uncertainties. At present, significant uncertainties still exist in observations, data assimilation, models, and computations (Melhauser & Zhang, 2012; Min & Wu, 2020). (b) Intrinsic predictability refers to the upper limit of atmospheric predictability under the

assumption that both initial conditions and models are nearly perfect (Lorenz, 1969; Rotunno & Snyder, 2008; Zhang et al., 2007).

It is widely accepted that the atmosphere has an inherent limit to its predictability, beyond which the developed error cannot be reduced, no matter how small the initial uncertainty is (Lorenz, 1969). For many years, scientists have been exploring the intrinsic predictability limits of the real atmosphere and error growth mechanisms. Generally speaking, many synoptic- or large-scale weather systems have a predictability period of about 2 weeks (Charney et al., 1966; Judt, 2018, 2020; Selz, 2019; Zhang et al., 2019). However, the predictability limit of mesoscale weather systems—ranging from hours to days—remains a contentious issue without a unified conclusion. Many studies have employed "twin experiments" (Bei & Zhang, 2014; Zhang et al., 2003, 2006, 2007) to analyze the growth of small-amplitude initial errors, which are found to grow at very high rates and exhibit "upscale growth" characteristics. The intrinsic predictability limits of different meteorological variables also represent an urgent scientific challenge. For example, Bei and Zhang (2014) studied variable- and scale-dependent error growth within a typical midlatitude cyclogenesis system using idealized moist baroclinic wave simulations. Their results demonstrated that in general, the variables with more small-scale components (such as vertical velocity) are less predictable, and vice versa (such as pressure). Ying and Zhang (2017) further investigated the predictability of multi-scale weather and convection-coupled equatorial waves during active Madden–Julian oscillation (MJO) events, and they found that the intrinsic predictability limits of horizontal wind, temperature, and specific humidity exceed 10 days for scales >500 km. For scales <100 km, the limits are less than 1 day. Notably, it can be revealed by both above-mentioned studies that precipitation exhibits more limited predictability compared to many other variables. Additionally, research has shown that the equatorial region demonstrates a longer predictable time than mid-to high-latitudes (Judt, 2020; Reynolds et al., 1994).

Research on atmospheric intrinsic predictability has gradually shifted from merely exploring predictability limits to investigating the fundamental dynamic mechanisms of error growth (Yang, 2011). Many studies have shown that error growth depends on moist convection processes (Bei & Zhang, 2007; Ehrendorfer et al., 1999; Sun & Zhang, 2016; Zhang et al., 2006). Based on the idealized moist baroclinic wave simulations, Tan et al. (2004) demonstrated fundamental differences between dry and moist dynamics in mesoscale predictability. The stronger the moist convective instability, the faster the error growth. Rapid error growth will not occur without latent heat release. Zhang et al. (2007) further utilized the above-mentioned idealized numerical simulations with improved model setup and proposed a three-stage error-growth conceptual model. Stage 1 (i.e., the initial convective growth stage) is dominated by convective instability, where small-scale errors grow rapidly and reach local saturation. Stage 2 (i.e., the intermediate adjustment stage) involves the transition of errors from convective-scale unbalanced motions to large-scale balanced motions, with geostrophic adjustment occurring through the convergence (or divergence) of inertia-gravity waves. Stage 3 (i.e., the large-scale growth stage) features slower growth of saturated errors in the large-scale balanced component under baroclinic instability.

Atmospheric energy spectra (i.e., atmospheric energy distributions across different scales or wavenumbers) and their underlying physical mechanisms have also long been a hot research topic, helping to advance understanding of the dynamic structure of multi-scale atmospheric motions as well as atmospheric intrinsic predictability limit. It has been identified repeatedly in observation data (e.g., Lindborg, 1999; Nastrom & Gage, 1985; Nastrom et al., 1984; Zhang et al., 2015), full-physics models (e.g., Skamarock, 2004; Skamarock et al., 2014; Waite & Snyder, 2013), and high-resolution reanalysis (Li et al., 2023) that the atmospheric energy spectrum (mostly the horizontal kinetic energy spectrum and available potential energy spectrum) often follows a k^{-3} power law at large scales, transitioning to a $k^{-5/3}$ power law at mesoscales, where k is the horizontal wavenumber. Currently, it is widely accepted that the formation mechanism of large-scale energy spectra with a slope of -3 could be explained by the quasi-geostrophic (QG) turbulence theory (Charney, 1971), but the mechanisms behind mesoscale energy spectra with a slope of $-5/3$ remain a highly controversial scientific issue (Peng et al., 2014; Zhang et al., 2024). The proposed explanations include a two-dimensional inverse energy cascade (Kraichnan, 1967) and a three-dimensional direct energy cascade (Kolmogorov, 1941). Increasing studies suggest that mesoscale kinetic energy spectra result from the combined effects of multiple mechanisms at different heights or scales, such as gravity waves and moist convection (Sun et al., 2017; Waite & Snyder, 2013; Wang et al., 2018). Theoretically, the spectral region preserving the $k^{-5/3}$ slope is often interpreted as the inertial range within which the energy input from larger scales passes through the mesoscales to dissipation scales. For instance, Dewan (1979, 1997) argued that atmospheric gravity waves possess a similar inertial range, leading to the observed transition from the synoptic scale to the mesoscale. In particular, here the horizontal kinetic energy is

often decomposed into rotational and divergent components by many studies (e.g., Blažica et al., 2013; Li et al., 2023; Stephan et al., 2022; Waite & Snyder, 2013; Žagar, Jelić, et al., 2017) to give an approximate separation between the balanced mode (e.g., Rossby waves) and the unbalanced mode (e.g., inertia–gravity waves), which helps to reveal the underlying physical mechanism behind the spectra.

Previous studies suggest that whether a flow has finite or infinite predictability is determined by the kinetic energy spectrum slope of the basic flow (Lorenz, 1969; Rotunno & Snyder, 2008). Studies using simplified turbulence models implies that flows have limited predictability as their energy spectrum follows a power law close to $k^{-5/3}$, while there is no such a limit for those following a power law close to k^{-3} (Leith & Kraichnan, 1972; Lorenz, 1969; Métais & Lesieur, 1986; Rotunno & Snyder, 2008). Such a theory has been supported by many studies when applied to an idealized and real atmosphere (Judt, 2018; Morss et al., 2009; Sun et al., 2017). However, recent studies suggest other possibilities for the relationship between the background energy spectrum slope and the intrinsic predictability limit, indicating that the precise nature of their connection remains elusive. For example, Lloveras et al. (2022) found that mesoscale predictability in idealized moist midlatitude cyclones is not sensitive to the slope of the background kinetic energy spectrum throughout the 36-hr simulations.

As an important subject in many research areas including atmospheric energy spectra and atmospheric intrinsic predictability, gravity waves (GWs) are ubiquitous buoyancy oscillations in stably stratified fluids, which profoundly interact with atmospheric processes at various spatiotemporal scales. Consequently, research on GWs provides critical insights into atmospheric physical mechanisms. Primary sources of atmospheric GWs are topographic forcing (e.g., Li & Chen, 2017; Queney, 1948; Smith, 1980; Yang et al., 2026), moist convection (e.g., Du et al., 2024; Fovell et al., 1992; Lane & Zhang, 2011; Lane et al., 2001; Wei, 2026; Yang & Du, 2024, 2026), jet-front system-related flow imbalance (e.g., Chasteen & Koch, 2022; Uccellini & Koch, 1987; Wei & Zhang, 2014, 2015; Zhang, 2004), and shear instability (e.g., Bretherton, 1988; Lin & Chun, 1991). As key components of mesoscale motions, GWs can contribute significantly to building the atmospheric energy spectra (Bierdel et al., 2016; Callies et al., 2014; Knobloch et al., 2023; Sun et al., 2017). Also, GWs are found to likely link small-scale errors at the initial stage to rapid upscale error growth and thus intrinsically limit mesoscale predictability (Bierdel et al., 2018; Sun & Zhang, 2016; Zhang et al., 2007).

GWs are often coupled with moist convection to eventually form banded convective systems in many observed weather events (e.g., Bosart et al., 1998; Clarke, 1972; Du & Zhang, 2019; Koppel et al., 2000; Ruppert et al., 2022, 2024; Zhou et al., 2024), but the intrinsic predictability of this weather phenomenon is rather underexplored. The interaction between waves and convection is complex. While GWs can initiate and modulate convection, the strong diabatic heating within active convective cores can, in turn, substantially alter the wave amplitude, phase relationships, and propagation properties (Koch et al., 1988; Ruppert et al., 2022). Despite these local modifications, the mesoscale wave signal often remains identifiable and crucial for the maintenance of the convective system. On 30 January 2018, multiple northwest-southeast oriented wavelike convective bands occurred near the south coast of China, lasting nearly 10 hr Du and Zhang (2019) (hereafter, "DZ19") simulated the convective event reasonably well, and they found it closely related to mesoscale GWs with a wave phase speed of around 12 m/s and a primary wavelength of ∼40–50 km, under the combined influence of the wave-duct mechanism and the wave-convection interaction. Building on this dynamic framework, Du et al. (2021) studied the practical and intrinsic predictability of this event through convection-permitting ensembles. They pointed out that the practical predictability depends on the correct initial state in terms of thermodynamics, and to a lesser degree on physical parameterizations. Furthermore, the pattern of wave-convection coupled bands is generally intrinsically predictable (forecast lead time <∼12 hr), but the phase of wavelike bands is intrinsically unpredictable after a short integration time (∼7 hr). Although the studies mentioned above on this GWs event have been conducted, many important aspects on its intrinsic predictability remain unknown, especially for the error growth behaviors and intrinsic predictability limits of different model forecast variables at different scales (in terms of different wavenumber or wavelength), and their connection with corresponding background (reference) spectra. As an extension of DZ19 and complementary to Du et al. (2021), this study seeks to further quantify the intrinsic predictability of different forecast variables at various scales through spectral analysis of the difference between perturbed and unperturbed convection-permitting simulations under varying degrees of initial moisture conditions.

The rest of this article is structured as follows. Section 2 reviews the basic information on the discussed wave-convection coupled bands from the published work, as well as a detailed introduction on the methodology

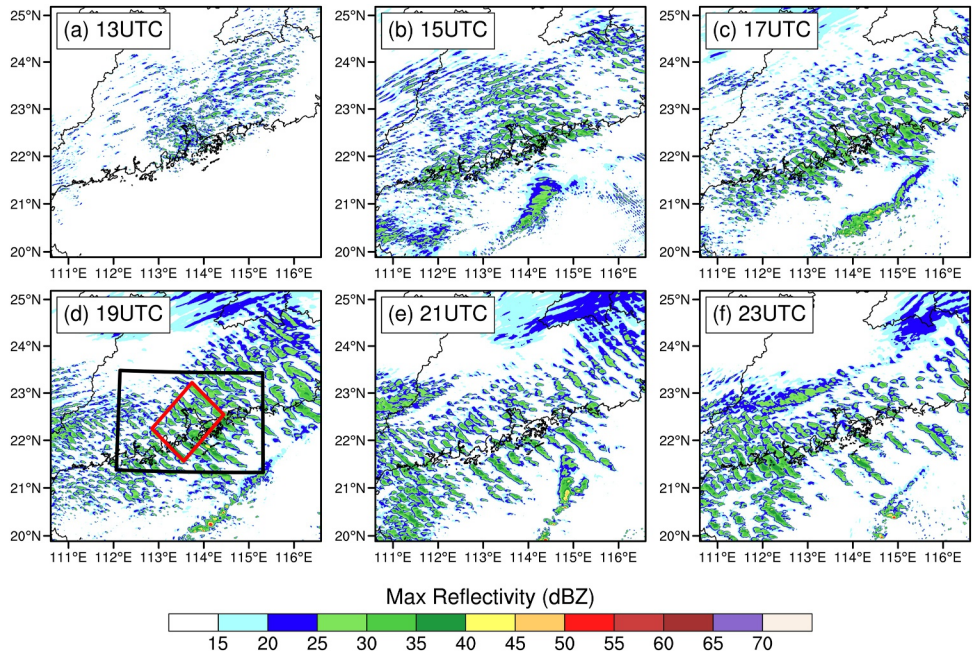

Figure 1. Simulated radar composite reflectivity at (a) 1300 UTC, (b) 1500 UTC, (c) 1700 UTC, (d) 1900 UTC, (e) 2100 UTC, and (f) 2300 UTC 30 January 2018 in the control (CNTL) run. The red box in (d) shows where the vertical cross sections of Figures 6 and 12 are interpolated. The black box in panel (d) is used in the computation of Figures 10, 15 and 17, 18. Please refer to Figure 2a (inner box d03) for the geographic context and domain boundaries. Adapted from Du and Zhang (2019, their Figure 6).

utilized in the current study. The scale- and variable-dependent error growth and predictability are investigated in Section 3. Section 4 explores the sensitivity of the error growth to the initial moisture content. Error growth of divergent and rotational kinetic energy is discussed in Section 5. Section 6 contains a summary and discussion.

2. Methodology

2.1. Case Overview

On 30 January 2018, multiple convective bands could be observed through the radar composite reflectivity derived from operational weather radars over Guangdong Province in South China, which was located on the cold side of a southwest-northeast oriented surface cold front with prevailing northeasterly winds near the surface (Figure 4 of DZ19). As reported in DZ19, this banded convective activity persisted for approximately 10 hr from 0800 to 1800 UTC 30 January 2018, featuring a westerly jet at 500 hPa centered near 25°N and a southwest-northeast oriented shear line at 850 hPa located at the north edge of Guangdong Province. The 850-hPa level exhibited strong southerly flow accompanied by pronounced vertical wind shear in the lower troposphere.

The convection-allowing simulation in DZ19 successfully captured the wavelike pattern of convective bands with horizontal wavelength (~40–50 km) and wave speed (~12 m/s) consistent with the radar observations in general, although the occurrence of the simulated wave pattern was delayed by a few hours (~5 hr) and its exact location tended to be more to the south (ocean side). As shown in Figure 1, the simulated convective system initially developed at 1300 UTC on 30 January, with distinct wavelike characteristics emerging between 1500 and 1700 UTC. At around 1900 UTC (Figure 1d), the wave signal became most significant, exhibiting at least nine coherently propagating convective bands with northeastward motion. The inter-band spacing notably increased for several convective bands located over eastern Guangdong Province from 2300 UTC.

As mentioned in Section 1, the synergistic effects of the wave-duct mechanism and wave-convection interaction [or called "wave-CISK (conditional instability of the second kind) hypothesis"] may explain the longevity of the banded convective activity (DZ19). The wave-duct theory conceptualized by Lindzen and Tung (1976) provides a comprehensive framework for characterizing certain environments, which can effectively trap GWs in the lower

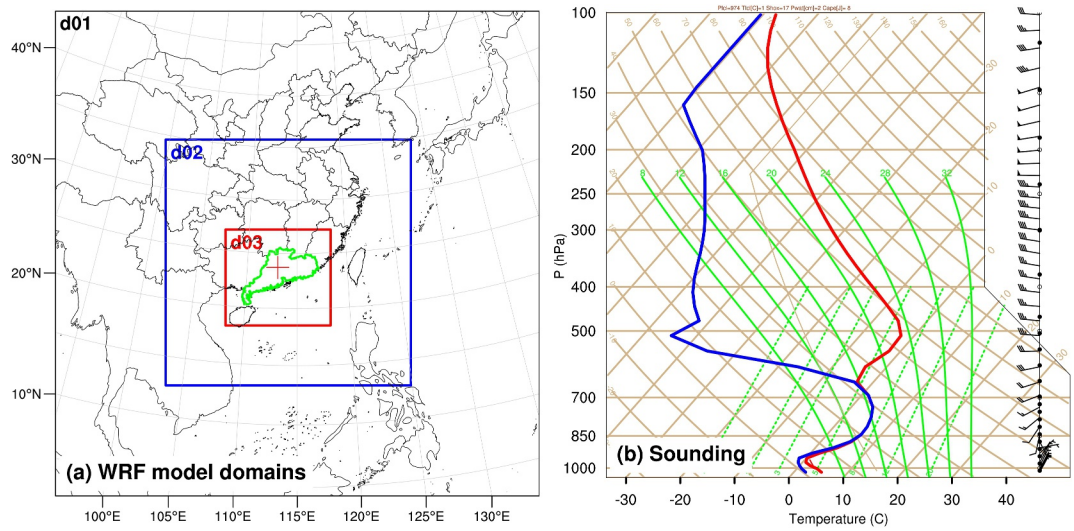

Figure 2. (a) WRF model domain configuration with map boundaries (contour). The one-way nested domains have horizontal grid spacings of 9 km (d01), 3 km (d02), and 1 km (d03). The Guangdong Province is indicated by green curves. (b) The skew T-log *p* diagram at Qingyuan at 1200 UTC 30 January 2018 from the CNTL run. The location of Qingyuan is indicated by the red cross in panel (a). Adapted from Du and Zhang (2019, their Figures 5 and 7).

troposphere through downward reflection while preventing energy loss in the vertical direction. As shown in Figure 2b, the simulated sounding agreed well with the observation (Figure 7b of DZ19), successfully reproducing the characteristic vertical stratification structure of the wave duct. Based on the quantitative diagnosis of moist Brunt-Väisälä frequency (N_m) (following DZ19), this structure is characterized by (a) a strong stable layer below 850 hPa (~1.5 km; excluding the surface layer), (b) a moist neutral stability layer within 850–600 hPa (~1.5–4.2 km) containing a critical level (~2.5 km; surrounded by a shallow layer with Richardson number <0.25), and (c) an upper stable layer within 600–500 hPa (~4.2–5.6 km). Together with the wave-duct theory, the wave-CISK mechanism can effectively explain the maintenance of long-lived wavelike convective bands (Powers & Reed, 1993; Zhang et al., 2001; DZ19). Wave-CISK describes the positive feedback process between moist convection and GWs. Specifically, GWs can trigger and regulate moist convection, directly influencing the convective bands. Meanwhile, the latent heat release generated by convection maintains and enhances GWs (Koch et al., 1988; Lindzen, 1974; Raymond, 1975).

2.2. Experimental Design

The Advanced Research Weather Research and Forecasting model (WRF Version 3.8.1; Skamarock et al., 2008) is employed in the present study to conduct unperturbed and perturbed cloud-permitting simulations, for the sake of revisiting the intrinsic predictability limit of the wave-convection coupled bands from a new perspective based on variable- and scale-dependent error growth. The model configuration of the unperturbed experiment or the control experiment (CNTL) follows that in the control run of DZ19. As depicted in Figure 2a, this study employed one-way nested domains with $\Delta x = 9$ km for domain 1 (d01), 3 km for domain 2 (d02), and 1 km for domain 3 (d03). The vertical grid contains 51 levels with the model top of 50 hPa where a 5-km absorbing layer of GWs is used. The Kain-Fritsch convection parameterization (Kain, 2004) is used in d01 but turned off in d02 and d03. The other physical parameterizations used in three domains include the Thompson et al. (2008) microphysics scheme, the Yonsei University boundary layer scheme (Hong et al., 2006), the Rapid Radiative Transfer Model for Global Climate Models (RRTMG) longwave-radiation and shortwave-radiation schemes (Iacono et al., 2008), the revised MM5 Monin-Obukhov surface-layer scheme (Jiménez et al., 2012), and the unified Noah land-surface-model scheme (Livneh et al., 2011). Following Bei and Zhang (2014, hereafter, "BZ14"), the perturbed experiment is designed by adding random, Gaussian noises with zero mean and a standard deviation of 0.2K to the potential temperature field at the initial time of the 9-km domain (d01) (hereafter referred to as CNTL-D1P). The main conclusions are insensitive to the choice of perturbed variable and the initial perturbation magnitude, provided that the perturbations are sufficiently small (not shown).

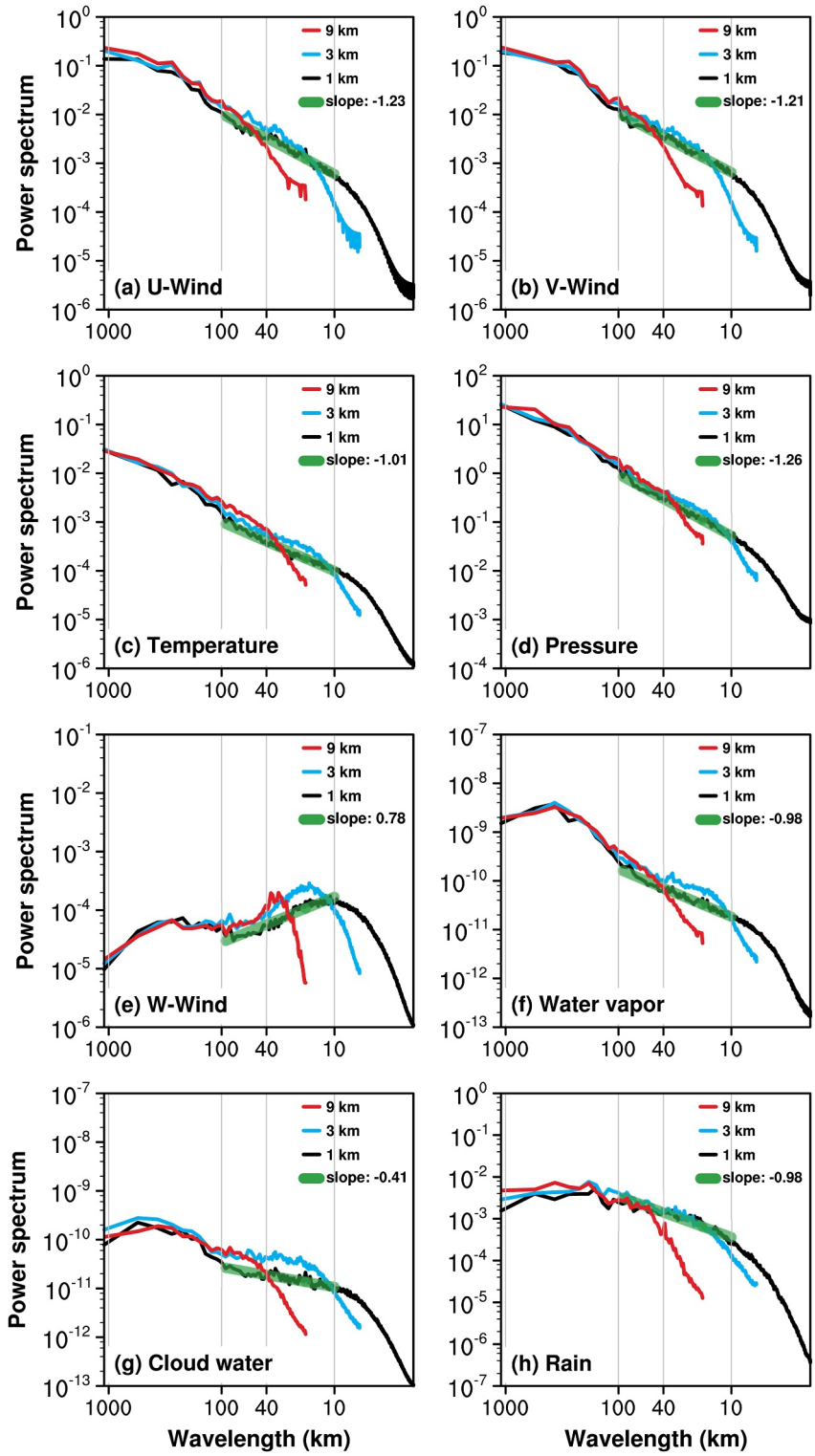

Figure 3. The reference (background) spectra of different variables at 1900 UTC, 30 January 2018 with the model grid spacings of 9, 3 and 1 km (red, blue and black thin, respectively) vertically averaged over 1–12 km across the same domain in the CNTL run, and the corresponding slopes (green bold) between 10- and 100-km wavelengths.

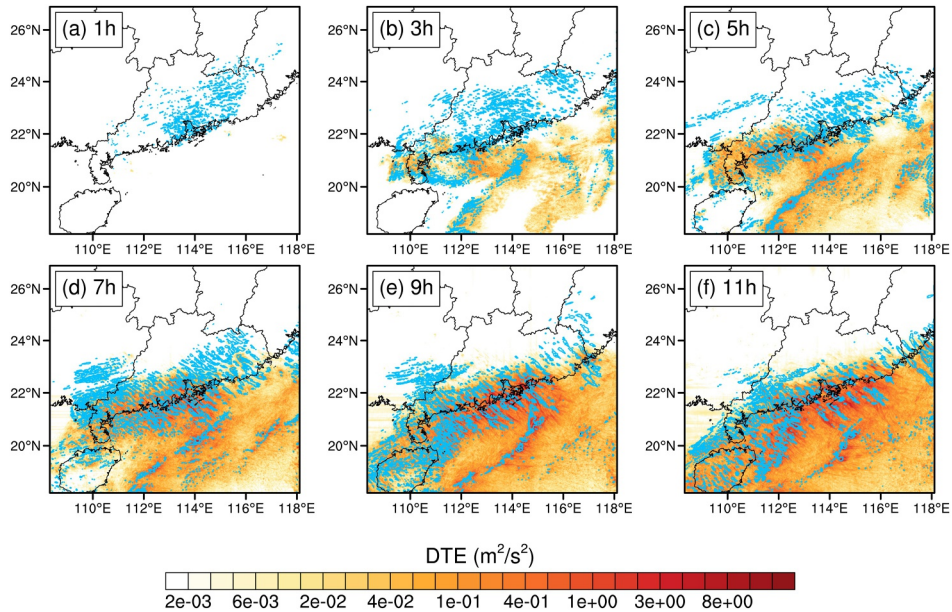

Figure 4. Horizontal distribution of difference total energy (shading; $m^2\ s^{-2}$) with the forecast lead time of (a) 1 hr, (b) 3 hr, (c) 5 hr, (d) 7 hr, (e) 9 hr, and (f) 11 hr from the full 1-km domain (d03) and vertically averaged over 1–12 km between the CNTL and CNTL-D1P runs. The blue contours denote the simulated radar composite reflectivity (≥25 dBZ, Δ = 5 dBZ) in the CNTL run.

To further test the sensitivity of error growth and intrinsic predictability to moist processes, several additional experiments (EXP80, EXP60, EXP40, and EXP20) (Tan et al., 2004; Wei & Zhang, 2014) are performed by reducing the initial water vapor mixing ratio at all grid points to a percentage (80%, 60%, 40%, and 20%, respectively) of CNTL. As for EXP00, in addition to setting the initial water vapor mixing ratio to zero, the convection parameterization scheme in d01, latent heating from microphysics and both sensible and latent heat fluxes from the surface are turned off, thereby establishing a perfectly dry atmospheric environment. The corresponding perturbed runs (EXP80-D1P, EXP60-D1P, EXP40-D1P, EXP20-D1P, and EXP00-D1P) are also conducted with the same initial perturbation added to d01 as in CNTL-D1P. All the simulations above are initialized at 1200 UTC on 30 January 2018.

The current article specifically tracks eight fundamental forecast variables, including zonal wind (u), meridional wind (v), temperature (T), pressure (P), vertical velocity (w), water vapor mixing ratio (q), cloud water mixing ratio (*cloud*), and 1-hr accumulated precipitation (*rain*). This selection follows BZ14, which allows a direct comparison with their work based on idealized moist baroclinic wave simulations.

2.3. Error and Predictability Metrics

Different from Du et al. (2021), the Loss Predictability Index (LPI, following BZ14) is applied to quantify the intrinsic predictability limit of each selected variable (e.g., u, T, and *rain*). The LPI is defined as the ratio of the forecast error (difference between perturbed and unperturbed) power spectrum to the reference (unperturbed) power spectrum at a given scale or within a range of scales. By definition, a larger value of the LPI indicates shorter predictability. Moreover, a 100% LPI indicates that the error power spectrum has reached its saturation limit (i.e., the corresponding reference power spectrum in CNTL). Results from idealized tests also show that, for a pure sinusoidal wave without amplitude error, a 100% LPI amounts to a shift of the phase by 1/6 of the wavelength (BZ14). Here in the current study, the useful prediction skill for any given variable is explicitly given by determining the forecast time at which the LPI reaches the threshold of 60% (Judt, 2018, 2020; Žagar, Horvat, et al., 2017).

The spatial error growth of the banded convection in a physical region can be examined quantitatively with classic grid point metrics by the difference total energy (DTE) formulated by Tan et al. (2004) and Zhang et al. (2003, 2007) as

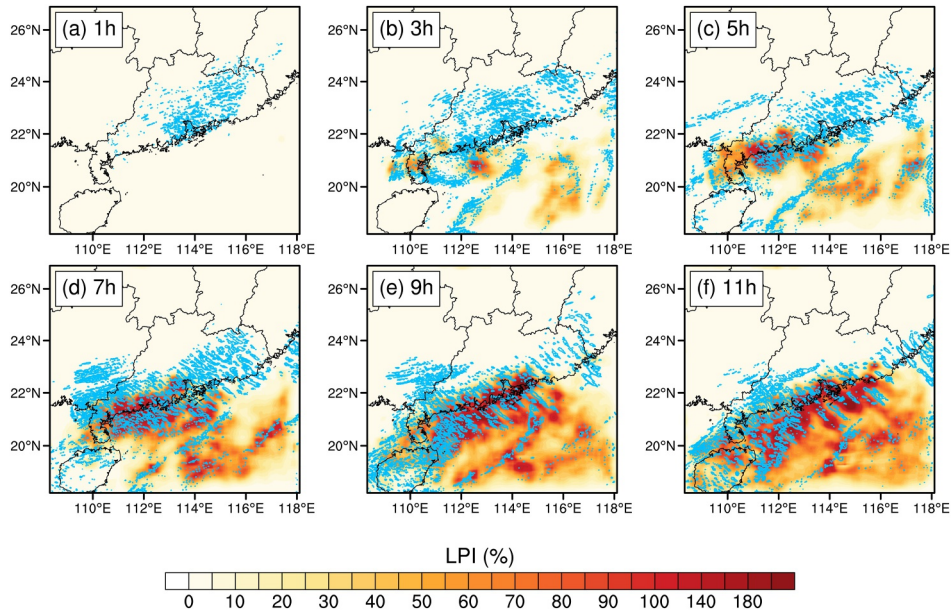

Figure 5. As in Figure 4, but for the horizontal distribution of LPI (the Loss Predictability Index, %).

$$\mathrm{DTE} = \frac{1}{2}\sum(u'u' + v'v' + \kappa T'T') \tag{1}$$

where u', v', and T' are the difference in wind components and temperature between the corresponding twin experiments, $\kappa = C_p/T_r$ ($C_p = 1005.7\ \mathrm{J\ kg^{-1}\ K^{-1}}$, which is the specific heat capacity, and $T_r = 270\mathrm{K}$, which is the reference temperature). $\sum$ represents the sum of the vertical and horizontal grid points of the 1-km domain (d03). Accordingly, the reference total energy [$\mathrm{TE} = \sum(U^2 + V^2 + \kappa T^2)/2$, where U, V, and T are wind components and temperature from the unperturbed runs] is introduced as part of the criterion for estimating predictability limit in the current study (which will be elaborated in the following paragraphs). By definition, DTE and TE are composite metrics integrating multiple conventional variables to characterize the holistic predictability.

Particularly for calculations in the physical field, the LPI of DTE (LPI-TE) is calculated as DTE/TE. A two-dimensional spatial filter (Appendix in Wei et al., 2016) is implemented to extract the small-scale component with horizontal wavelengths <200 km. The DTE at scales smaller than 200 km represents the errors from mesoscale GWs and convective instability of interest in the current case (Du et al., 2021). Additionally, building upon the flux computation methodology of Wei et al. (2016), the LPI-TE derivation here employs a 40-km spatial smoothing. Sensitivity calculations with varying spatial smoothing windows (e.g., 200 km vs. 40 km) are also conducted and give similar results in general (not shown).

2.4. Reference Power Spectra Over the Entire Domain

Using the two-dimensional spectral analysis obtained by discrete Fourier transforms (DFT, section b of the appendix in Wei et al., 2016), this subsection first introduces and compares the power spectral characteristics of eight selected forecast variables in CNTL, which provide prerequisite information on the reference or background power spectra for the intrinsic predictability investigation in the following sections. The bi-directional linear detrending is applied before performing DFT, which is a procedure conducted by many studies (Errico, 1985; Errico & Baumhefner, 1987; BZ14) in order to better satisfy the assumption of doubly periodic lateral boundary conditions made in the computation of DFT for regional data sets. Although the above detrending method attenuates the spectral variance of the largest scales [$k < \sim 4$ in this study; $k < \sim 2$ in Denis et al. (2002)], tests show no significant sensitivity at the scales of interest discussed in the current study.

Table 1
Reference Spectral Slopes Between 10- and 100-km Wavelengths at 1900 UTC, 30 January 2018 in Unperturbed Experiments

	BZ14	CNTL	EXP80	EXP60	EXP40	EXP20	EXP00
u	−1.91	−1.23	−1.33	−1.49	−1.48	−1.47	−1.41
v	−1.73	−1.21	−1.28	−1.35	−1.35	−1.34	−1.29
T	−1.96	−1.01	−1.09	−1.15	−1.14	−1.13	−1.09
P	−2.05	−1.26	−1.30	−1.34	−1.33	−1.32	−1.32
w	0.67	0.78	0.92	0.76	0.77	0.77	0.79
q	−1.65	−0.98	−1.38	−1.66	−1.74	−1.78	NaN
cloud	−1.50	−0.41	−0.34	−1.66	−0.38	0.10	NaN
rain	−1.68	−0.98	−0.93	−1.90	−0.24	0.96	NaN

Note. The spectra are vertically averaged over 1–12 km across the full 1-km domain (d03). For variables that remain zero throughout the experiment, spectral slopes are undefined and thus recorded as NaN (Not a Number). Note that the slopes from BZ14 (Bei & Zhang, 2014) are between 20- and 200-km wavelengths.

Figure 3 shows the reference spectra of eight selected variables at 1900 UTC, 30 January 2018 (when the wave signal became most significant) vertically averaged over 1–12 km from the CNTL run. The upper and lower boundaries are chosen to minimize interference from both surface topography and sponge layer effects. Note that altering the above ceiling altitude at 12 km by ±2 km sensitivity range does not lead to major changes in the conclusions, as verified in the tests (not shown). By identifying the wavelength where the spectrum begins to decay relative to a higher-resolution spectrum, the effective resolution (Skamarock, 2004; BZ14) is around five to seven times the model grid spacing, indicating weakly variable-dependent characteristics (Figure 3). The slopes of reference power spectra between 10- and 100-km wavelengths of the investigated variables differ significantly, but are all close to or shallower (i.e., flatter in the spectrum) than −5/3. More specifically, pressure has the steepest power-spectrum slope (−1.26), while *w* has the shallowest (and a positive) slope (0.78). The spectral slopes of *u*, *v* and pressure (−1.23, −1.21 and −1.26, respectively) are relatively close to −5/3 [a typical mesoscale power spectral slope value found in many studies, for example, Nastrom & Gage, 1985; Skamarock et al., 2014; Sun & Zhang, 2016]. The spectral slopes of temperature, water vapor, cloud water and *rain* (−1.01, −0.98, −0.41 and −0.98, respectively) are much shallower than −5/3. Ying and Zhang (2017) also demonstrated a much shallower spectral slope of the precipitation spectrum (compared to their kinetic energy spectrum).

Compared to BZ14's work based on the idealized moist baroclinic wave simulations (Table 1), all eight variables in the current study have shallower spectral slopes. Nonetheless, the ranking of slope magnitudes across variables remains generally consistent with BZ14. As discussed in BZ14, the shallower the reference spectrum, the more instabilities at the smaller scales. Therefore, the shallower slopes in this case may be primarily attributed to the active mesoscale dynamics (e.g., ducted gravity waves) inherent to the environment, with moist convection exerting a secondary shallowing effect. Specifically, by further dividing the troposphere into a lower layer (1–6 km, containing the three-layer wave-ducting structure introduced in Section 2.1) and an upper layer (6–12 km), the contributions of active mesoscale dynamics and moisture can be more clearly demonstrated (Figure S1). The lower layer (1–6 km) displays significantly shallower slopes than the upper layer (6–12 km) in both moist and dry runs. This persistence confirms that ducted wave dynamics fundamentally drive the energetic mesoscale motions even without moisture. Meanwhile, the inclusion of moisture leads to slightly flatter slopes and higher spectral amplitudes for most variables. Kouhen et al. (2024) also found that convection and orography have a shallowing effect on the mesoscale kinetic energy spectrum. While it is beyond the scope of this study to provide comprehensive analyses that lead to conclusive evidence regarding topographic influences, their potential effects cannot be excluded and will be examined in detail separately in future research.

3. Scale- and Variable-Dependent Error Growth and Predictability

This section provides a comprehensive analysis of the error growth between CNTL and CNTL-D1P from the perspective of physical and spectral space, quantifying the intrinsically predictable time scale of each forecast variable via the LPI defined in Section 2.3.

3.1. Error Growth in Physical Space Over the Entire Domain

Figures 4 and 5 present a basic overview of the horizontal distribution of vertically averaged DTE and LPI-TE at different forecast lead times over the entire 1-km domain (d03), respectively. As shown in Figure 4, during the first 3 hr, the initially minuscule DTE amplifies primarily within oceanic convective cells before propagating rapidly to the surrounding areas. The expanding error field soon permeates the marine atmospheric column of the 1-km domain. By 5 hr, land-based errors exhibit rapid development, closely following the propagation of wavelike convective bands (traveling with mesoscale GWs). After 8 hr, the horizontal diffusion rate of DTE shows marked deceleration. Generally speaking, oceanic DTE maintains greater magnitude and spatial coverage compared to its terrestrial counterpart. This land-sea contrast is likely attributed to the stabilizing effect of the colder land surface and the deterministic anchoring by topography (Judt, 2020), which tend to suppress the

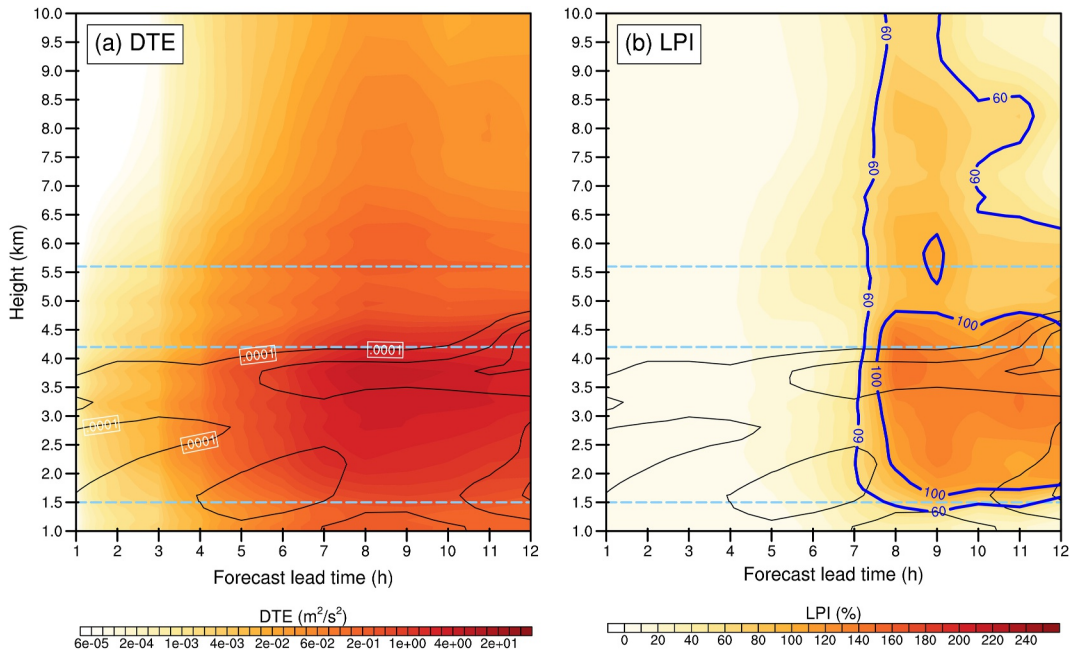

Figure 6. Temporal evolution of averaged vertical cross sections of (a) DTE (shading; $m^2\ s^{-2}$), (b) LPI (shading; %) and cloud water mixing ratio (black contour; kg kg^{-1}) compositing (averaging) along the horizontal wave propagation in the red box of Figure 1d. The blue contours in panel (b) denote 60% and 100% LPI. DTE and LPI are calculated from the CNTL and CNTL-D1P runs, while the cloud water mixing ratio is derived from the CNTL run. Light-blue dashed lines demarcate the wave-ducting stratification, which features: a strong stable layer below 850 hPa (∼1.5 km; excluding the surface layer), a moist neutral stability layer within 850–600 hPa (∼1.5–4.2 km), and an upper stable layer within 600–500 hPa (∼4.2–5.6 km).

stochastic error growth relative to the moist, unstable marine environment. Despite this disparity, the DTE maxima remain well correlated with the locations of banded convections in both maritime and continental regions. The horizontal DTE propagation in the current case closely resembles the tropospheric error growth process over the first 24 hr reported by Judt (2018). Since the horizontal distribution of TE (that is, the denominator in the computation of LPI-TE; Equation 1) is relatively uniform (Figure S2), the evolution of the peak areas in LPI-TE is generally consistent with that in DTE (especially over the convective regions; Figure 5).

As to the vertical direction, Figure 6 shows the temporal evolution of averaged vertical cross sections of DTE and corresponding LPI-TE along the horizontal wave propagation in the red box of Figure 1d. The detailed calculation procedure consisted of two steps: (a) vertical cross-section interpolation within the red box of Figure 1d, followed by (b) directional averaging parallel to the convective band propagation at each forecast lead time.

As illustrated in Figure 6, during the initial 7-hr period, DTE displays rapid quasi-exponential growth, while its development in the upper-level troposphere above the wave-ducting structure (>5.6 km) lags approximately 3 hr behind the lower levels. DTE growth rates decrease after 7 hr of forecasting. The LPI-TE above 1.5 km altitude reaches the 60% threshold between 7 and 8 hr. The intrinsic predictability timescale derived above shows close agreement with the timescale of the vertically integrated DTE after applying the 200-km high-pass filtering (∼7 hr) reported by Du et al. (2021, their Figure 19). Notably, the moist neutral stability layer attains 60% threshold slightly earlier than the upper levels (>4.2 km). Additionally, the vertical distribution of DTE displays pronounced variation, while this vertical gradient gradually weakens with increasing forecast lead time. Both DTE and LPI-TE peak within the moist neutral stability layer, particularly within the 2.5–4.2 km layer (i.e., above the critical layer), which achieves 100% LPI prior to 8 hr.

3.2. Error Growth in Spectral Space

3.2.1. Domain-Wide and Vertically Averaged Error Growth

Spectra of DTE and TE with different grid spacings vertically averaged over 1–12 km are compared in Figure 7. The increasing spacing among adjacent green thin lines at different time steps (Δ = 1 hr) in Figure 7 indicates

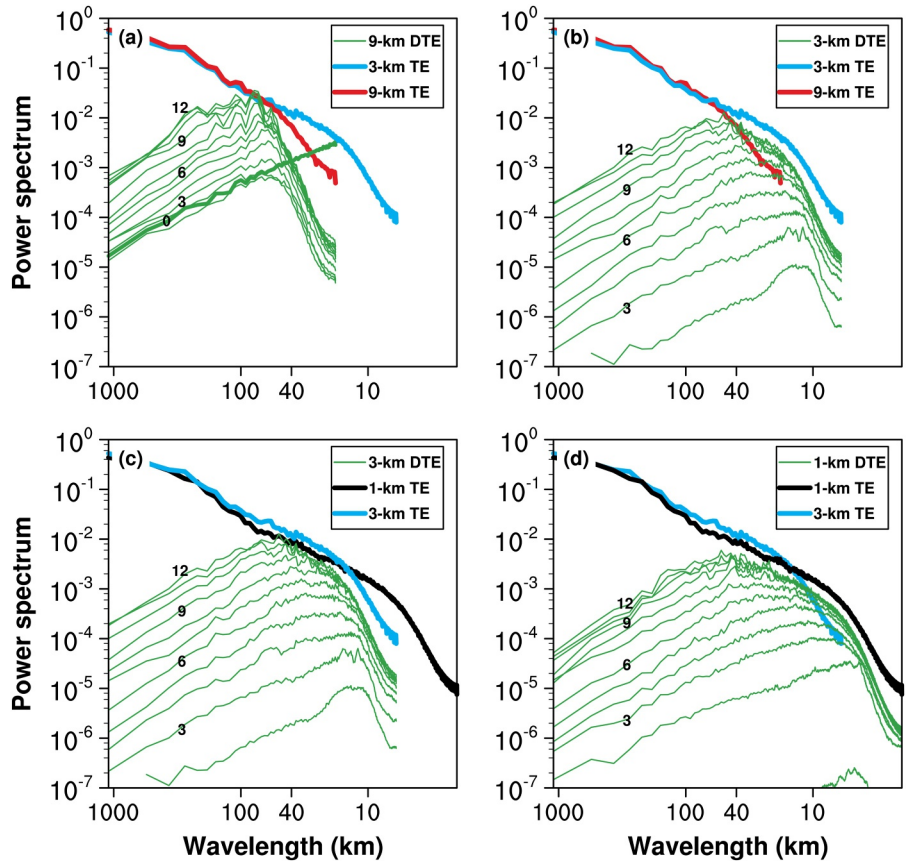

Figure 7. (a, b) Spectra of DTE (green thin) and TE (bold) with grid spacings of 9 and 3 km (red bold: 9 km; blue bold: 3 km). (c, d) Spectra of DTE (green thin) and TE (bold) with grid spacings of 3 and 1 km (blue bold: 3 km; black bold: 1 km) vertically averaged over 1–12 km across the same domain between the CNTL and CNTL-D1P runs. The green lines (lower to upper) denote the difference spectra between lead times of 1 and 12 hr at 1-hr intervals. The time sequence is denoted as digital numbers in the figures. The 0-hr DTE spectrum in panel (a) is highlighted with a thick line.

accelerated error growth. As in Tan et al. (2004) and Zhang et al. (2007), the spectral density of the initial white noise (added only to the potential temperature field) is proportional to the horizontal wavenumber (Figure 7a). Over the first 1-hr period, DTE at the smallest scales (<70 km; Figure 7a) decreases sharply, largely due to model diffusion (Snyder et al., 2003; Tan et al., 2004; Wirth & Ghil, 2000; Zhang et al., 2007). Subsequently, DTE grows at a relatively slow rate across the scales above the effective resolution ($\sim 7\Delta x$). The spectrum of DTE calculated in the domain with the 9-km grid spacing (9-km DTE) peaks at scales near the effective resolution. However, the spectral peak exhibits negligible migration toward larger scales over 12-hr simulation. As shown in Figures 7a and 7b, during the first several hours, the error grows more rapidly at smaller scales and spreads to larger scales more quickly before the error saturates at those small scales in the 3-km domain in comparison with that of the 9-km domain. Similar results can be found in the comparisons between the 3-km and 1-km domains, but with less distinction. These findings are generally consistent with the conclusions drawn in BZ14. Over the same 1-hr interval, the spectral peaks of 3-km and 1-km DTE (Figures 7c and 7d) exhibit systematic upscale shifts, consistent with the concurrent increases in both the scale of differences variation and their spatial extent (Figure 4; Tan et al., 2004). Overall, the domain with higher resolution can better resolve more vigorous small-scale instabilities, and LPI-TE reaches 60% earlier at smaller scales compared with larger scales (Figure 7).

Figure 8 shows the error and reference spectra of 8 selected variables over the entire 1-km domain vertically averaged over 1–12 km. The error growth characteristics of these eight variables not only mirror the 1-km DTE evolution pattern demonstrated in Figure 7d but also conform to the theoretical framework of upscale error growth under −5/3 spectral slope conditions in background flows as established by Rotunno and Snyder (2008). Regardless of the initial perturbation scales and amplitude, the error spectra consistently converge toward the

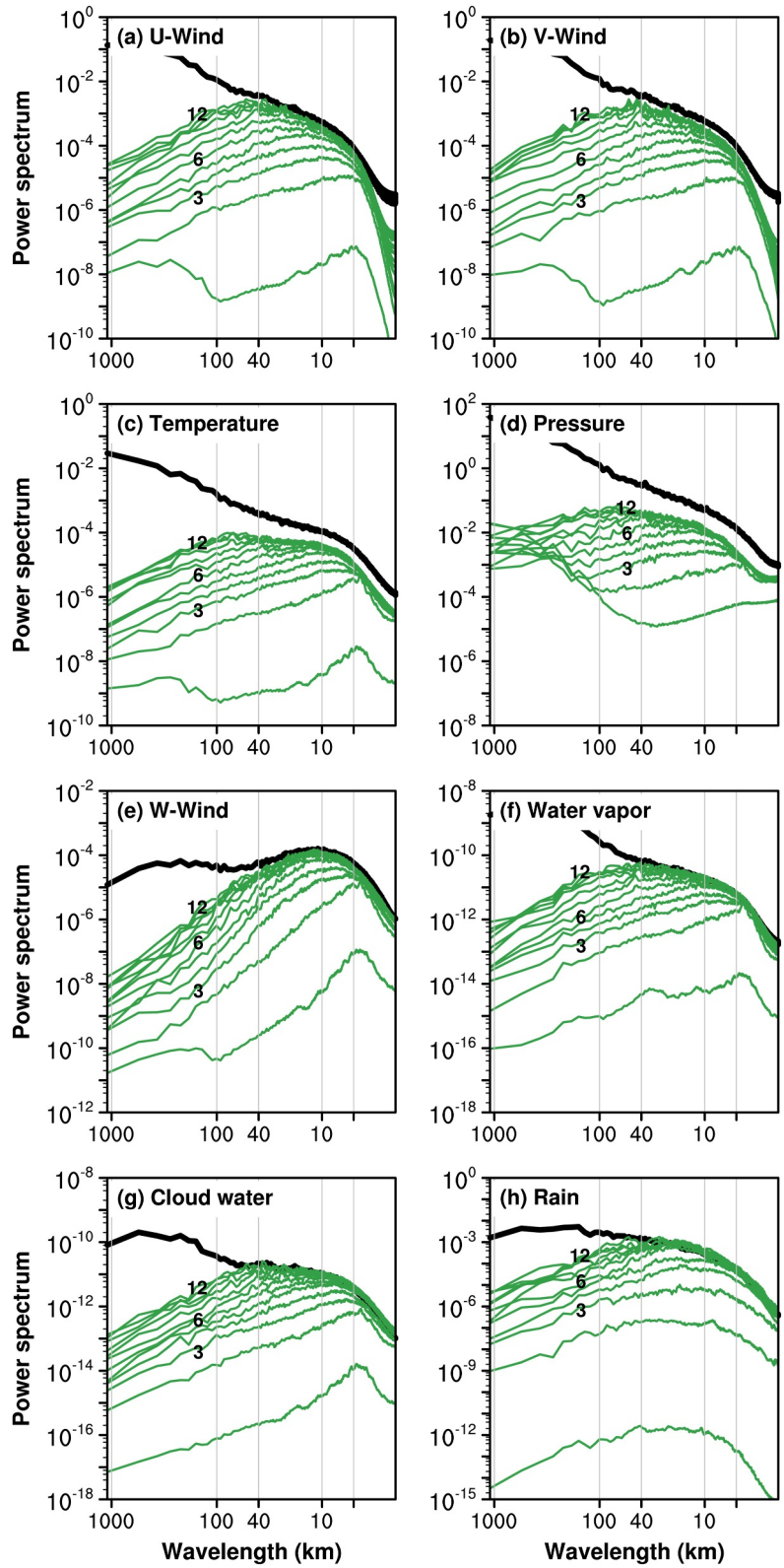

Figure 8. As in Figure 7, but for different variables over the entire 1-km domain (d03). The vertical gray solid line at ~5 km wavelength in each subplot denotes the corresponding effective resolution.

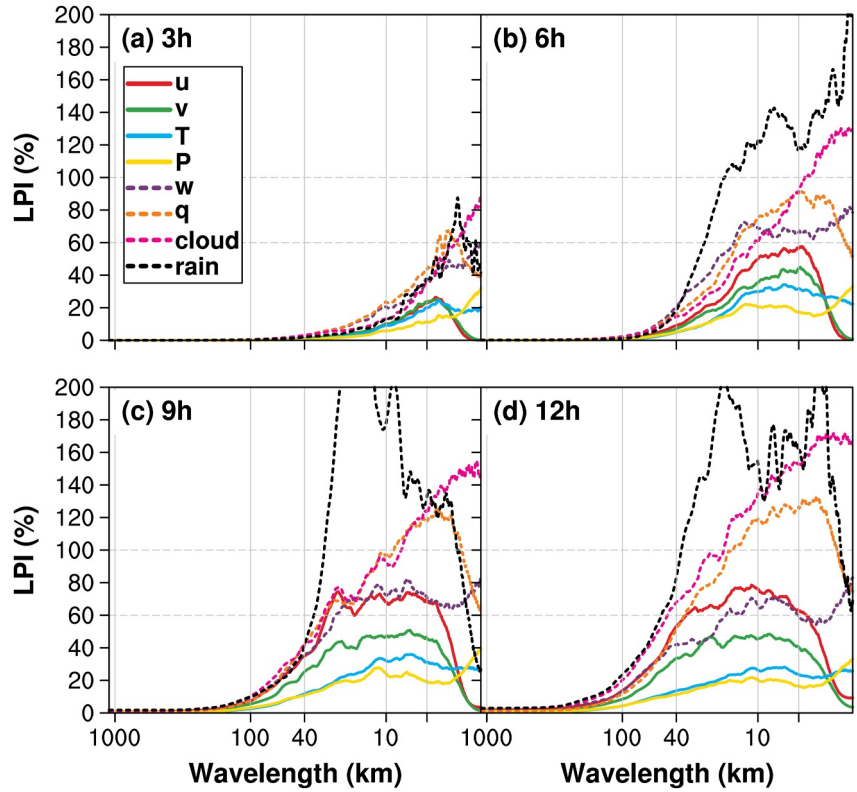

Figure 9. Spectral distribution of LPI (%) for the variables zonal wind (red solid), meridional wind (green solid), temperature (blue solid), pressure (yellow solid), vertical velocity (purple dashed), water vapor mixing ratio (orange dashed), cloud water mixing ratio (pink dashed), and 1-hr accumulated precipitation (black dashed) with the forecast lead time of (a) 3 hr, (b) 6 hr, (c) 9 hr, and (d) 12 hr vertically averaged over 1–12 km from the full 1-km domain (d03) between the CNTL and CNTL-D1P runs. The horizontal gray dashed lines denote 60% and 100% LPI. The vertical gray solid line at ~5 km wavelength in each subplot denotes the corresponding effective resolution.

slopes of the reference spectra (Sun & Zhang, 2016). However, compared with other variables, *T* and *P* demonstrate significantly slower error growth rates and can hardly attain their saturation thresholds.

Through the analysis of the spectral distribution of LPI from the entire 1-km domain, Figure 9 provides a clearer visualization of significantly variable-dependent error saturation characteristics across different scales. Variables directly related to moist convection (such as *w*, *q*, *cloud*, and *rain*) demonstrate a higher degree of error saturation with LPI reaching 60% at earlier stages (<6 hr). This rapid error saturation is further corroborated by the analysis of simulated radar composite reflectivity (Figure S3), which exhibits an error evolution pattern consistent with other hydrometeors. *u* attains the threshold during later stages (~7 hr), whereas *v*, *T* and *P* fail to reach their 60% threshold across all scales within the simulation period. It is revealed by the comparison with the reference spectral slopes in Section 2.4 that variables exhibiting shallower reference spectral slopes generally demonstrate higher degrees of error saturation or less predictability. Additionally, the high values of LPI first appear at smaller scales, and these high-value windows in the LPI spectra for all variables widen toward larger scales over time, which also demonstrates the consistent convergence of the error spectral slopes toward the reference spectra.

3.2.2. Region- and Altitude-Dependent Localized Error Growth in Convective Bands

Further investigation of scale-dependent predictability limits in the rest of the subsection focuses on two representative wavelengths: 10 km (representing the smallest resolvable convective cells and the lower limit of predictability) and 40 km (primary horizontal wavelength of the banded convection), with particular attention to the variable-dependent predictable time at these scales. Besides, by focusing on the localized convective bands (black box in Figure 1d) and two distinct lower-tropospheric layers, a more thorough investigation on the role of moist convection in error growth and height-dependent intrinsic predictability can be achieved. Based on the

vertical stratification structure of the wave duct mentioned in Section 2.1, two representative altitudes are selected, including 3 km within the moist neutral stability layer and 1.3 km within the ducting stable layer.

Figures 10a and 10b show the evolution of LPI at the scales of 10 and 40 km for 8 variables vertically averaged over 1–12 km from the entire 1-km domain. For the LPI threshold at 60% (hereafter the same for all variables), at the 10-km scale, *rain* exhibits the shortest predictability timescale (~4 hr). The variables *w*, *q*, and *cloud* show intermediate predictability durations of 5–6 hr, while *u* reaches approximately 7 hr. In contrast, the variables *v*, *T*, and *P* demonstrate significantly longer predictability limits exceeding 12 hr. At the 40-km scale, only *rain* and *cloud* attain the thresholds within 8 and 12 h respectively, whereas all other variables exceed 12-hr predictability limits. More limited intrinsic predictability of precipitation relative to other variables such as horizontal wind, temperature and humidity is consistent with Ying and Zhang (2017). The shorter predictability timescales at smaller scales compared to larger scales further validate the conclusions drawn in Figure 9.

Figures 10c and 10d display the evolution of vertically averaged LPI for the eight selected variables within localized convective bands (black box in Figure 1d). At the scale of 10 km, the eight variables exhibit predictability timescales of 5–6 hr, with a significant increase in LPI (i.e., more limited predictability) for *v*, *T*, and *P*. At the scale of 40 km, the predictable time of *rain* reduces to 6–7 hr, while other variables demonstrate further reduced timescales of 7–9 hr.

Figures 10e–10h show significantly higher localized LPI values and shorter predictability timescales over the moist neutral stability layer (3-km altitude) compared to the ducting stable layer (1.3-km altitude). This altitude-dependent predictability primarily stems from the fundamentally different dynamical stability governing each layer (Ruppert et al., 2022). Specifically, the moist neutral layer (3 km) serves as the primary locus for the vigorous release of moist convective instability (not shown). Consequently, variables in this layer suffer from rapid error saturation driven by chaotic convective overturning (i.e., "Stage 1" error growth; Zhang et al., 2007), which leads to a rapid loss of intrinsic predictability. In contrast, the 1.3-km layer is characterized by static stability, which is essential for the wave-ducting mechanism. Despite being coupled to the convection above via low-level convergence, this stable layer acts as a wave duct that favors organized, coherent wave propagation. This stabilizing nature allows the low-level flow to retain predictability longer than the moist neutral stability layer above. It is found that the eight studied variables become more correlated under the coupling between GWs and convection, leading to converged (i.e., more coherent) predictability characteristics. Furthermore, Judt (2020) demonstrates that topographic effects likely account for the enhanced predictability timescales toward the surface, especially for mesoscale dynamical processes. A detailed investigation of these topographic influences on error growth will be conducted in future research.

In general, error growth exhibits pronounced region and altitude dependence, which is strongly correlated with moist convection processes. Specifically, in regions and vertical layers with the strongest moist convection, all variables demonstrate both the fastest error growth (or the shortest predictability) and the most consistent inter-variable predictability characteristics, especially compared with domain-wide and vertically averaged results. Furthermore, the magnitudes of different power components in CNTL positively correlate with their corresponding LPI growth rates among variables, which suggests that large-amplitude reference power spectra may be associated with large instability and fast error growth for the corresponding variable.

4. Sensitivity to Initial Moisture Content

To rigorously examine the impact of initial moisture content on the reference power spectra and error growth, this section employs paired sets of sensitivity experiments (EXP80, EXP60, EXP40, EXP20, and the extremely dry EXP00) and their corresponding perturbed counterparts for systematic analysis.

Figure 11 shows the reference power spectra of 8 variables at 1900 UTC vertically averaged over 1–12 km from the entire 1-km domain (d03) in unperturbed runs with varying initial water vapor values. The corresponding spectral slopes between 10- and 100-km wavelengths are listed in Table 1. It is evident that the sensitivity of the power spectrum to initial moisture conditions varies substantially across different variables. Concretely speaking, the variables of *cloud* and *rain* exhibit the most pronounced spectral modifications, demonstrating substantial spectral power attenuation at all scales and a transition from negative to positive spectral slopes as moisture decreases. The spectra of *q* exhibit the secondary pronounced adjustments. From the CNTL to the EXP00 run, the magnitude of its spectral power attenuation gradually diminishes across 5 km (i.e., $5\Delta x$) to 100 km wavelengths,

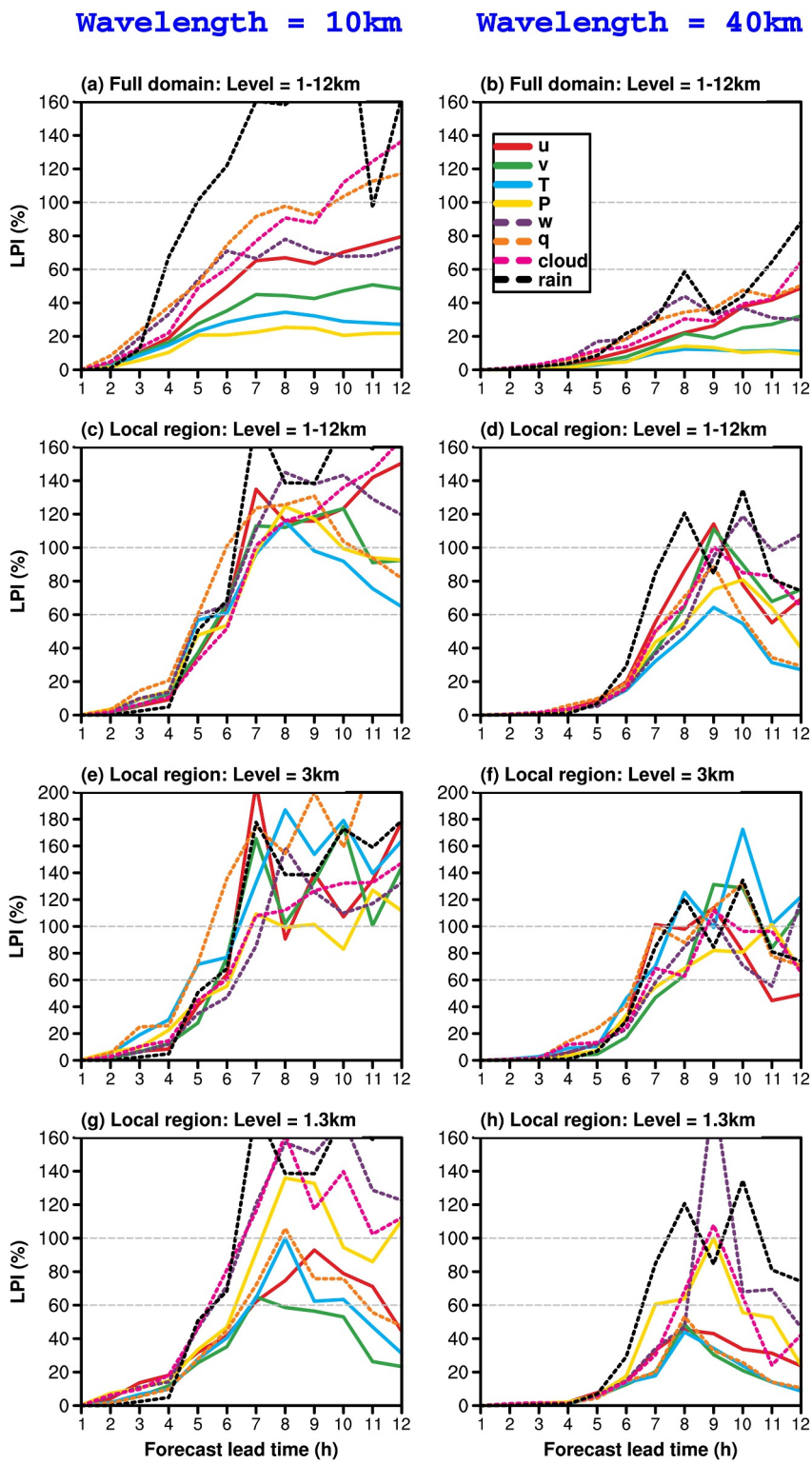

Figure 10. (a–d) Temporal evolution of LPI (%) at the scales of 10 and 40 km for different variables vertically averaged over 1–12 km from (a, b) the full 1-km domain (d03) and (c, d) the black box of Figure 1d between the CNTL and CNTL-D1P runs. (e–h) LPI evolution for the localized variables in the black box of Figure 1d specifically at (e, f) 3.0 km and (g, h) 1.3 km altitudes. The horizontal gray dashed lines denote 60% and 100% LPI.

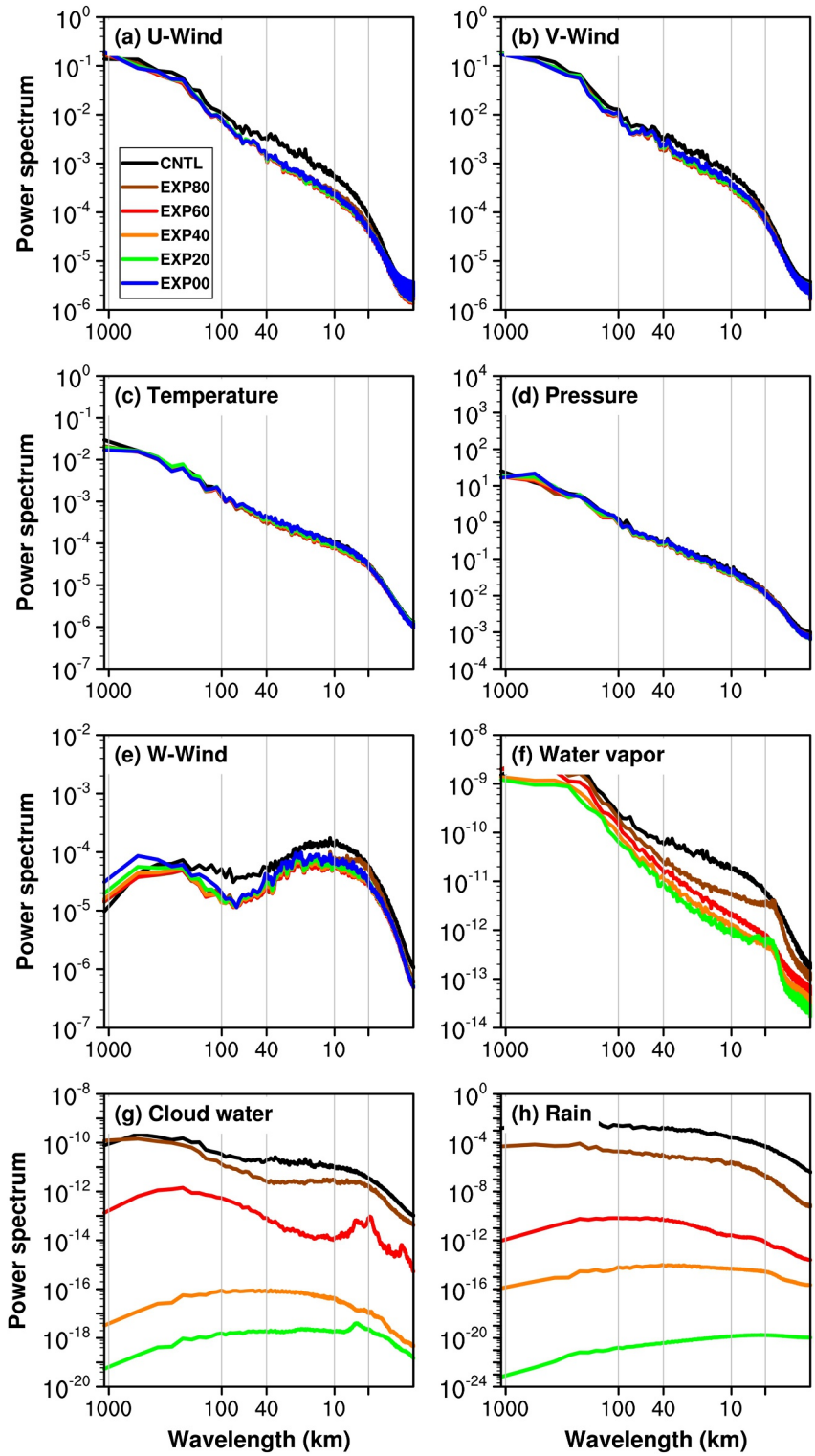

Figure 11. The reference (background) spectra of different variables at 1900 UTC, 30 January 2018 vertically averaged over 1–12 km from the full 1-km domain (d03) in unperturbed runs with varying initial water vapor values. Note that water vapor, cloud water, and 1-hr accumulated rain remain identically zero throughout the EXP00 run. The vertical gray solid line at ~5 km wavelength in each subplot denotes the corresponding effective resolution.

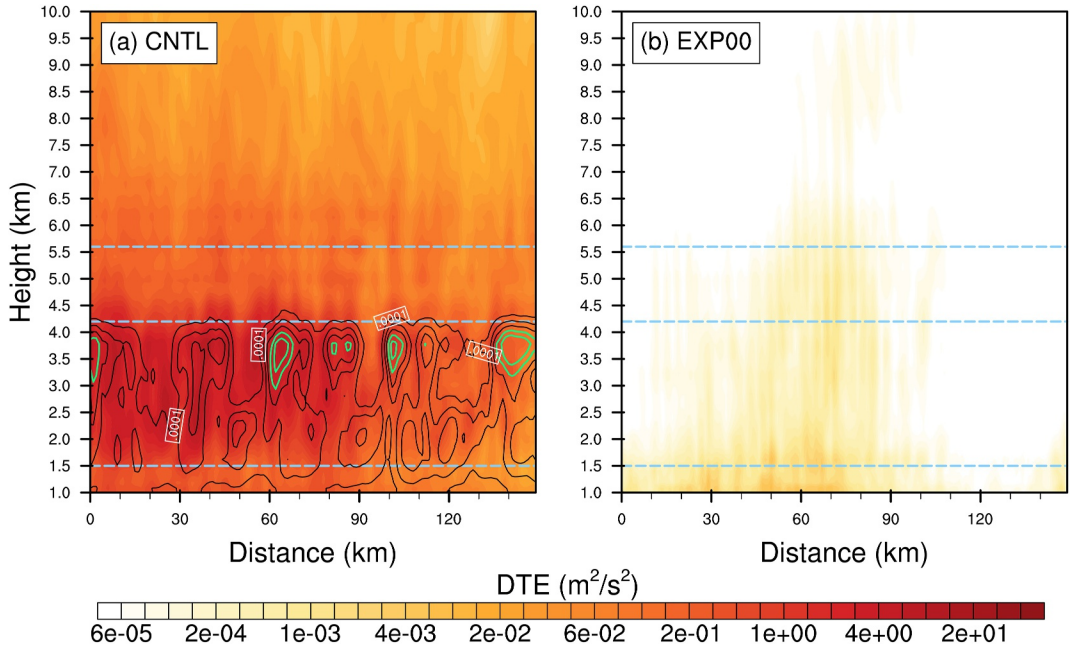

Figure 12. Vertical cross sections of DTE (shading; $m^2\ s^{-2}$) compositing (averaging) along the horizontal wave propagation in the red box of Figure 1d with the forecast lead time of 7 hr (1900 UTC) from the 1-km domain (d03). DTE in panel (a) is calculated from the CNTL and CNTL-D1P runs, while DTE in panel (b) is calculated from the EXP00 and EXP00-D1P runs. The cloud water mixing ratio (contour; kg kg^{-1}) in panel (a) is derived from the CNTL run. Light-blue dashed lines demarcate the wave-ducting stratification. The left (right) side of x axis is the southwest (northeast) side. Note that the cloud water mixing ratio remains identically zero throughout the EXP00 and EXP00-D1P runs.

leading to the monotonic steepening fitted spectral slope. Moreover, the energy spectra of wind components (i.e., u, v, and w) show significant attenuation from the CNTL to the EXP80 run across the scale range between 5 km (i.e., $5\Delta x$) and 100 km. Further moisture reduction from 80% to 0% produces negligible changes in the spectra of all three wind components. Slopes of horizontal and vertical kinetic energy spectra in EXP00 are either slightly steeper than or comparable to that in CNTL. The results here support the findings of Hamilton et al. (2008) that dry simulations exhibit mesoscale kinetic energy spectra with both weaker amplitudes and steeper slopes compared to corresponding moist-physics simulations. In contrast, the reference spectra of temperature and pressure exhibit negligible sensitivity to the initial moisture content.

For error growth analysis, EXP00 and EXP00-D1P are selected as representative experiments. In the horizontal distribution, the vertically averaged DTE (Figure S4) exhibits significantly smaller error growth compared to the CNTL experiment (i.e., Figure 4). Figure 12 compares the vertical cross sections of DTE along the horizontal wave propagation between EXP00 and CNTL twin experiments at the forecast lead time of 7 hr (1900 UTC), revealing fundamentally distinct vertical error distribution characteristics between dry and moist experiments. The error magnitude in the dry experiment is significantly smaller than in CNTL, with errors primarily concentrated near the surface and diminishing with height. This contrasts sharply with the CNTL results (Section 3.1) in which DTE maxima consistently align with the moist neutral stability layer and exhibit strong spatial correlation with convective bands.

In the wavenumber space, spectra of DTE and TE vertically averaged over 1–12 km for the EXP00 twin experiments are shown in Figure 13. Direct comparison with Figure 7 reveals that moist processes primarily modulate the spectral distribution of DTE rather than TE. Under dry conditions, the DTE magnitude and growth rates across all three horizontal resolutions exhibit significant reduction. While Figure 13a maintains a consistent white noise signal with prior results (i.e., a spectral profile proportional to wavenumber, as shown in Figure 7a at 0 hr), the subsequent temporal evolution of 9-km DTE reveals a noticeable decay of the initial error, which is likely attributable to sub-grid perturbation growth dominated by model diffusion in the absence of resolved convective instability. As shown in Figures 13c and 13d, the spectral growth of 3-km and 1-km DTE exhibits a pronounced bimodal structure, with one peak near the effective resolution scale (consistent with previous

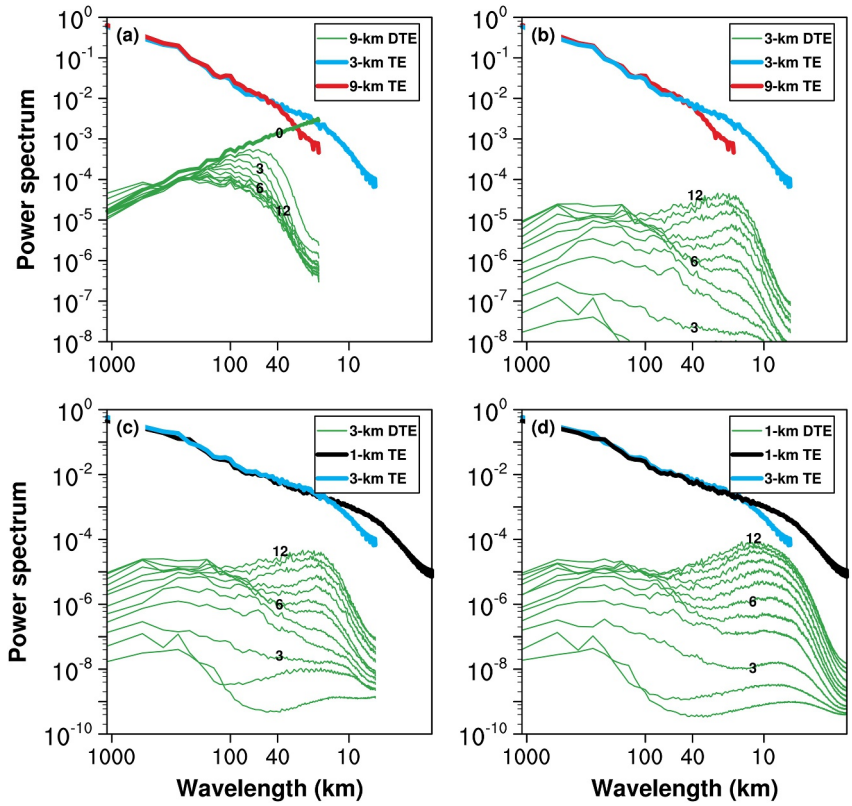

Figure 13. As in Figure 7, but for the spectra of DTE (green thin) and TE (bold) between the EXP00 and EXP00-D1P runs. The 0-hr DTE spectrum in panel (a) is highlighted with a thick line.

findings) and another peak at wavelengths exceeding 100 km. This pattern likely results from significantly suppressed small-scale error growth without convective instability, leading to comparable energy amplification rates between the smaller scales (<40 km) and larger scales (>100 km). This interpretation might be supported by the horizontal wind error growth shown in Figure 8, where the horizontal wind error spectra initially exhibit a similar bimodal structure, and then adjust to a unimodal distribution within 1 hour due to rapid small-scale error growth, ultimately converging toward the reference energy spectrum slope. Furthermore, the power spectra of 1-km DTE (Figure 13d) grow at nearly the same rate across all scales during the first 10 hr, which might resemble the "up-amplitude" error growth characteristics (Rotunno et al., 2023; also seen in Figure 11a of Sun and Zhang (2016)). Throughout the 12-hr simulation, DTE maintains an increasing trend across all scales, and it has not yet reached the saturation limit (i.e., the corresponding TE in EXP00).

Figures 14 and 15 provide more intuitive visualizations of the intrinsic predictability differences between dry and moist simulations through quantitative LPI metrics. Specifically, Figure 14 displays the spectral distribution of LPI vertically averaged over 1–12 km from the entire 1-km domain at the end of the simulation (0000 UTC), while Figure 15 shows temporal evolution of localized LPI at 10-km wavelength over two selected vertical layers. The vertically averaged reference power spectra of the variables u, v, T, P and w in EXP00 exhibit slopes either nearly identical to or slightly steeper than CNTL (Table 1). However, the predictability timescales are uniformly extended beyond 12 hr with LPI maintaining exceptionally low values regardless of scale, region, or altitude. This suggests an intricate relationship between the reference power spectral slope and intrinsic predictability. Besides, unlike Figures 10e and 10g, Figure 15 no longer displays height-dependent characteristics closely associated with the wave-ducting stratification structure.

The aforementioned analysis, in conjunction with Tan et al. (2004) and Zhang et al. (2003, 2007), gives a further demonstration that moist convection plays an essential role in organizing and amplifying small-scale small-amplitude perturbations over the early stages of the simulations.

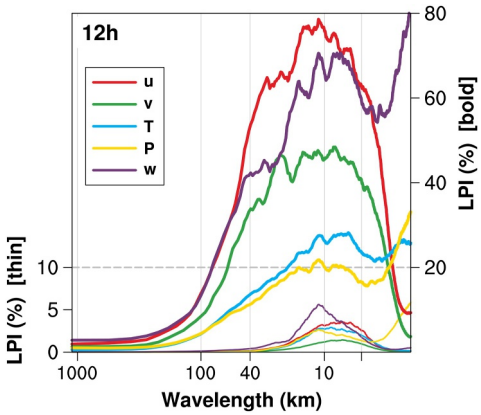

Figure 14. As in Figure 9d, but the thin (bold) lines show the spectral distribution of LPI (%) for variables from the full 1-km domain (d03) between the EXP00 (CNTL) and EXP00-D1P (CNTL-D1P) runs. The vertical gray solid line at ~5 km wavelength denotes the corresponding effective resolution.

5. Error Growth of Divergent and Rotational Kinetic Energy

Deeper insights can be gained into the underlying dynamics of the wavelike banded convection by further decomposing the kinetic energy spectrum into horizontally divergent and rotational components, $E_D(k_h)$ and $E_R(k_h)$, which are defined by Sun et al. (2017) as:

$$\int E_D(k_h)\,dk_h = \iint \frac{1}{2}\overline{\rho}\frac{\{\boldsymbol{\sigma}\}\cdot\{\boldsymbol{\sigma}\}}{{k_h}^2}dk_x dk_y \tag{2}$$

$$\int E_R(k_h)\,dk_h = \iint \frac{1}{2}\overline{\rho}\frac{\{\boldsymbol{\xi}\}\cdot\{\boldsymbol{\xi}\}}{{k_h}^2}dk_x dk_y \tag{3}$$

where the horizontal wavenumber k_h is defined as ${k_h}^2 = {k_x}^2 + {k_y}^2$, $\boldsymbol{\sigma}$ and $\boldsymbol{\xi}$ are the horizontal divergence (*div*) and vertical vorticity (*rot*), respectively. In this way, the total wind (*tot*) spectra (i.e., the kinetic energy spectra) computed as the sum of the zonal and meridional velocity components are equivalent to the sum of divergent and rotational kinetic energy spectra (Blažica et al., 2013). Here, the divergent and rotational components can serve as proxies of wave and vortex energy (Zhang et al., 2024). The main question addressed in this section concerns the scale- and height-dependent contribution of divergent kinetic energy (i.e., unbalanced components or wave parts) to total kinetic energy, along with its connection with error growth under varying moisture conditions.

Figure 16 gives an overview of the reference spectra of *div*, *rot* and *tot* at 1900 UTC vertically averaged over 1–12 km from the entire 1-km domain in unperturbed runs with varying initial water vapor values. The corresponding slopes between 10- and 100-km wavelengths are summarized in Table 2. Consistent with the spectral evolution patterns of zonal and meridional velocity components concluded from Figure 11 and Table 1, the divergent and rotational kinetic energy spectra exhibit substantial attenuation from CNTL to EXP80 across the scale range between 6 km (i.e., $6\Delta x$ or the approximate effective resolution) and 100 km, while the divergent components display a relatively weaker decrease. Here, the vertically averaged mesoscale divergent kinetic energy spectrum is less sensitive to the initial moisture content compared to the rotational component. This sensitivity difference may be attributed to the distinct generation mechanisms of the two components. The mesoscale rotational kinetic energy (serving as a proxy for vortices) relies critically on the stretching of vorticity by convective updrafts, a process intrinsically driven by latent heat release. Consequently, reducing initial moisture directly removes the energy source required for these updrafts, leading to a drastic collapse of the rotational kinetic energy spectrum (Figure 16b). In contrast, the mesoscale divergent kinetic energy (characterizing inertia-gravity waves) persists relatively better even in drier conditions, likely sustained by buoyancy oscillations or transient imbalances. Therefore, while both components weaken in absolute terms, the divergent component suffers a much weaker attenuation (Figure 16a). Figure 16d further quantifies the relative contribution of divergent kinetic energy to the total kinetic energy spectra. In the CNTL experiment, rotational kinetic energy dominates across all scales above the effective resolution. However, due to the selective suppression of the rotational component described above, reducing initial moisture content leads to an enhanced relative contribution of divergent kinetic energy at wavelengths below 50 km, with divergent components even surpassing rotational kinetic energy near the scale of 10 km. Additionally, across all sensitivity experiments, the divergent kinetic energy

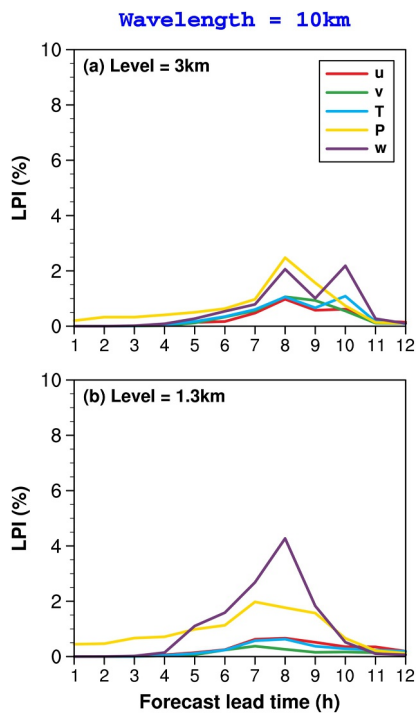

Figure 15. As in Figures 10e and 10g, but for the localized variables in the black box of Figure 1d specifically at (a) 3.0 km and (b) 1.3 km altitudes between the EXP00 and EXP00-D1P runs.

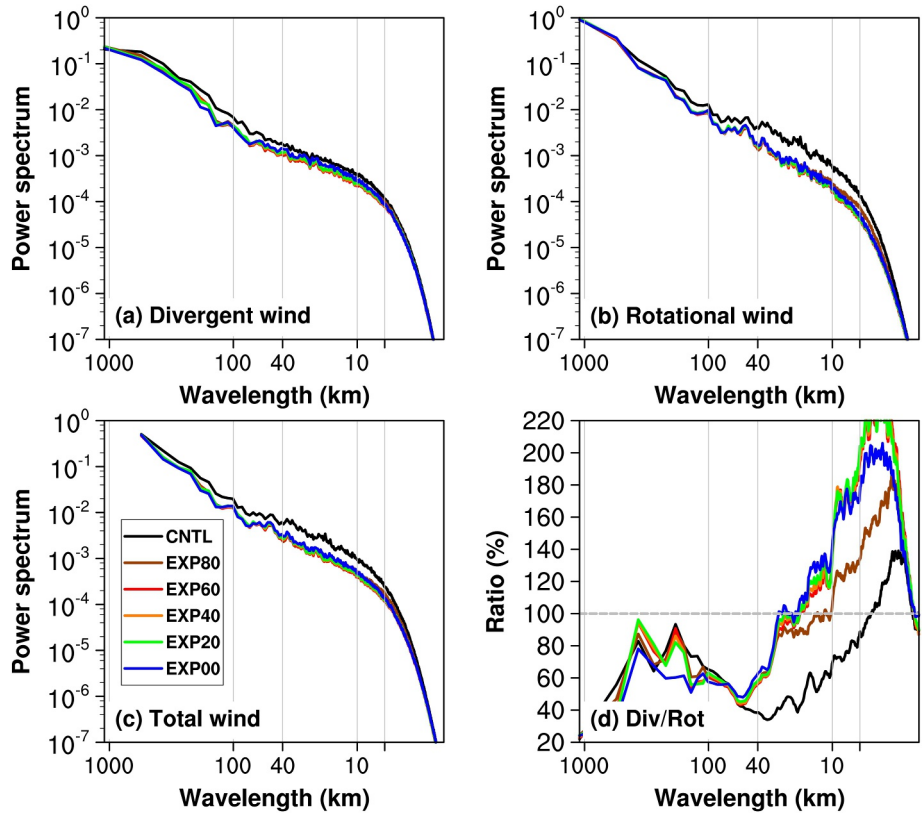

Figure 16. As in Figure 11, but for the variables (a) divergent wind, (b) rotational wind and (c) total wind. (d) The ratio (%) of the divergent to the rotational kinetic energy. The vertical gray solid line at ~6 km wavelength in each subplot denotes the corresponding effective resolution.

spectra exhibit much shallower slopes than the rotational kinetic energy spectra (Table 2), in agreement with the findings of Waite and Snyder (2013) and Blažica et al. (2013).

Figure 17 illustrates error spectra for divergent wind, rotational wind and total wind specifically at 3-km altitude within the moist neutral stability layer and at 1.3-km altitude within the ducting stable layer averaged over the localized convective bands (the black box of Figure 1d) for the dry and control experiments. The differences in error growth between dry and moist simulations align fundamentally with the characteristics described in Section 4. The elimination of initial moisture induces scale-dependent attenuation of reference background spectral amplitudes for divergent and rotational components at two selected altitudes, with more pronounced effects on the 10–40 km wavelength band. Within this wavelength band, the attenuation in the middle-level moist neutral stability layer is greater than that in the low-level ducting stable layer.

Figure 18 ultimately presents the LPI evolution of divergent and rotational wind as well as the ratio of the divergent kinetic energy to the rotational one. In the CNTL experiment (Figures 18a and 18b), the kinetic energy spectrum over the middle-level moist neutral stability layer is dominated by the rotational component. LPI of both *div* and *rot* exhibit similar growth rates across all scales, with LPI values at the smallest scales exceeding the 60% threshold after 5 hr. Over the low-level ducting stable layer with horizontally propagating GWs, the relative contribution of divergent components to the total kinetic energy is much larger compared with the moist neutral stability layer above. This is consistent with the theoretical assumption that the divergent component is closely linked with the gravity wave dynamics (or the unbalanced mode in general). Nonetheless, as both divergent and rotational kinetic energies are much weaker over the low-level wave ducting layer with a much dryer environment, both of their LPI values remain significantly lower

Table 2
Reference Spectral Slopes Between 10- and 100-km Wavelengths at 1900 UTC, 30 January 2018 in Unperturbed Experiments

	CNTL	EXP80	EXP60	EXP40	EXP20	EXP00
div	−1.08	−1.00	−1.05	−1.04	−1.04	−0.97
rot	−1.25	−1.39	−1.58	−1.57	−1.56	−1.51
tot	−1.20	−1.23	−1.35	−1.34	−1.33	−1.27

Note. The spectra are vertically averaged over 1–12 km across the full 1-km domain (d03).

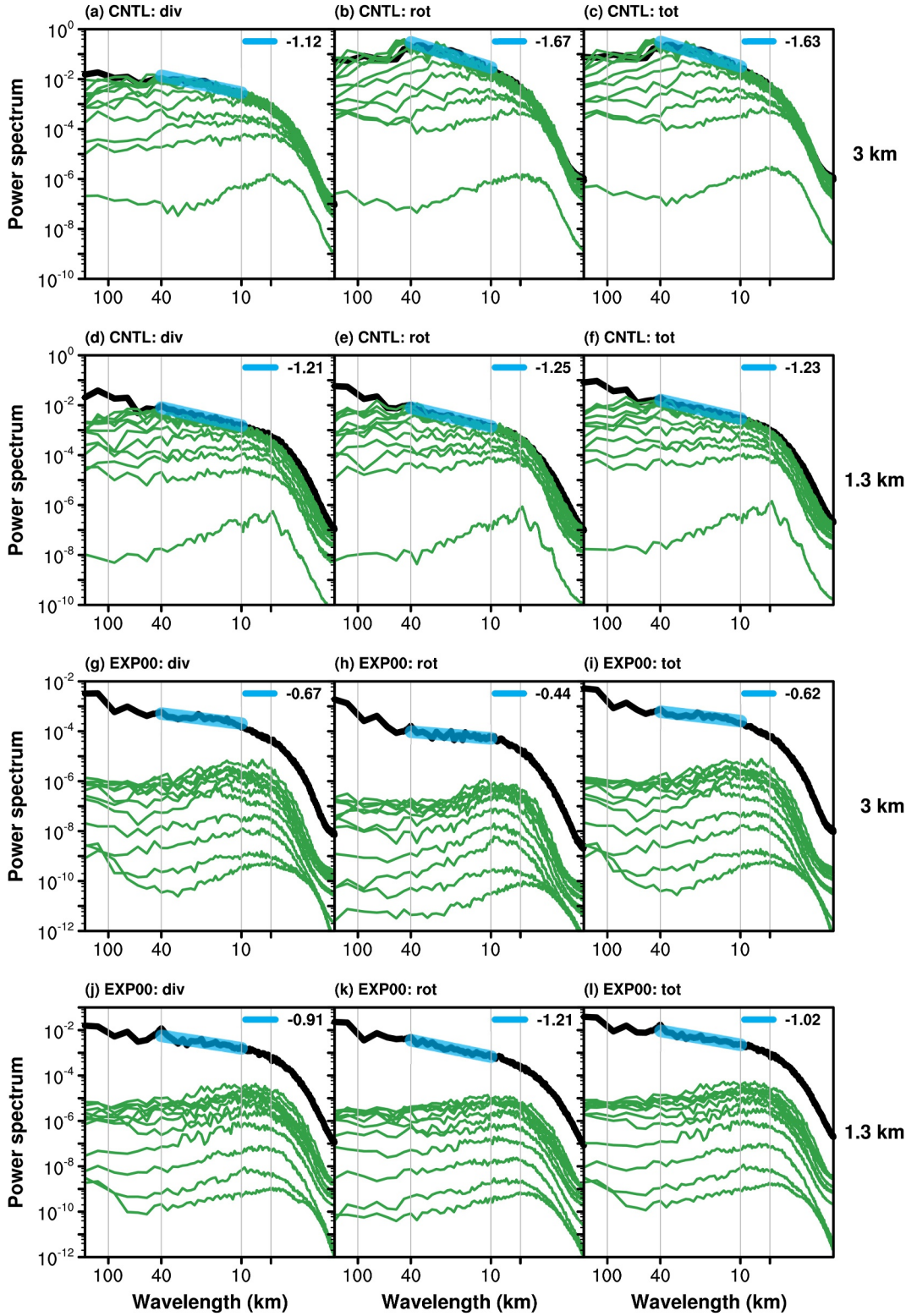

Figure 17. As in Figure 8, but for spectra of divergent wind, rotational wind and total wind specifically at (a–c, g–i) 3.0 km and (d–f, j–l) 1.3 km altitudes averaged over the black box of Figure 1d from the 1-km domain (d03) between the CNTL (EXP00) and CNTL-D1P (EXP00-D1P) runs. The legend values (upper right) denote the corresponding slopes (blue bold) between 10- and 40-km wavelengths. The vertical gray solid line at ~6 km wavelength in each subplot denotes the corresponding effective resolution.

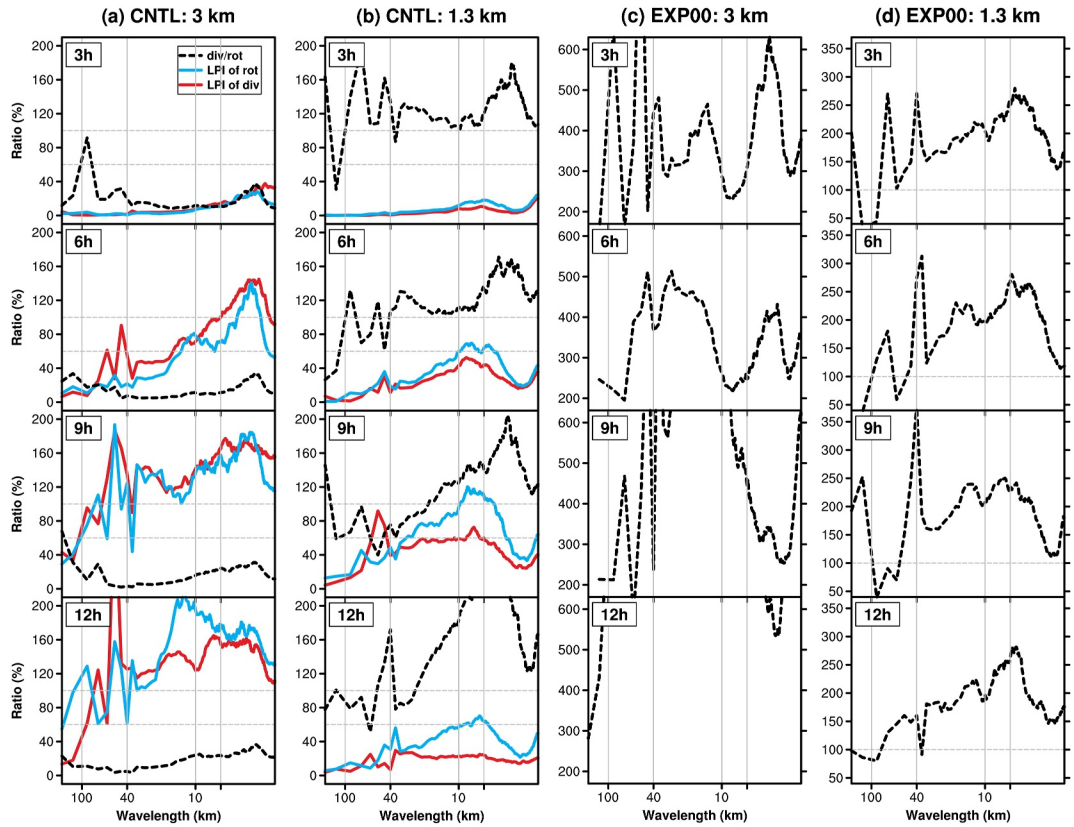

Figure 18. Spectral distribution of LPI (%) for divergent (red solid) and rotational wind (blue solid) and the ratio (%) of the divergent to the rotational kinetic energy (black dashed) specifically at (a, c) 3.0 km and (b, d) 1.3 km altitudes in the black box of Figure 1d from the 1-km domain (d03) between the CNTL (EXP00) and CNTL-D1P (EXP00-D1P) runs. The horizontal gray dashed lines denote 60% and 100% LPI (ratio). The vertical gray solid line at ~6 km wavelength in each subplot denotes the corresponding effective resolution.

compared with the moist neutral stability layer above. The height dependence of error saturation time is also found in Judt (2018), which similarly demonstrated a shorter predictable time for rotational versus divergent components at 850 hPa in the mesoscales. In the EXP00 experiment (Figures 18c and 18d), the divergent kinetic energy spectrum in the moist neutral stability layer grows to 4~6 times the amplitude of the rotational spectrum, while in the ducting stable layer this ratio remains approximately 200%. In addition, both height levels maintain exceptionally low LPI values (<2%).

Collectively, the divergent (unbalanced) and rotational (balanced) components of the mesoscale horizontal flow, which can serve as proxies of wave and vortex, demonstrate contrasting behaviors in the power spectrum, intrinsic predictability limit, and sensitivity to different initial moist contents. A reduction in initial moisture content weakens both divergent and rotational kinetic energy in wave-ducting structures, although the divergent component exhibits relatively smaller attenuation. Under this condition, the LPI growth rates for both energy components also decrease. Additionally, the moist neutral stability layer exhibits a more limited intrinsic predictability on *div* and *rot* variables compared to the ducting stable layer.

6. Conclusions and Discussion

In the current study, convection-permitting twin experiments with varying degrees of convective instability are conducted to revisit the variable- and scale-dependent intrinsic predictability of wave-convection coupled bands near the south coast of China on 30 January 2018 documented in DZ19. Different from Du et al. (2021), this study applies the Loss Predictability Index (LPI, following BZ14), defined as the ratio of the forecast error (difference between perturbed and unperturbed) power spectrum to the reference (unperturbed) power spectrum at a given scale or within a range of scales, to quantify the intrinsic predictability limit of each selected variable. This

quantitative framework allows for a rigorous re-examination of the error growth mechanisms (Figure S5), confirming that the limited intrinsic predictability of wavelike bands is primarily dominated by phase (location) uncertainty, which quantitatively corroborates the low intrinsic phase predictability originally suggested by Du et al. (2021).

Using the two-dimensional spectral analysis obtained by discrete Fourier transforms, this study compares the background power spectral characteristics of eight selected forecast variables. In the control (CNTL) run, the slopes of reference power spectra between 10- and 100-km wavelengths of the investigated variables differ significantly, but are close to or shallower than −5/3. More specifically, *P* has the steepest slope (−1.26), while *w* has the shallowest (and a positive) slope (0.78). Furthermore, moist convection has a shallowing effect on the mesoscale power spectrum of *u*, *v*, *T*, *P*, *q* variables in general.

The spatial distribution of error growth closely resembles the tropospheric error growth process over the first 24 hr reported by Judt (2018). The maxima of difference total energy remain well correlated with the banded convections in both maritime and continental regions. With the new procedure to strictly identify the intrinsic predictability limit, the derived timescale for the useful prediction skill shows close agreement with the timescale of the wavelike band phase (∼7 hr) reported by Du et al. (2021). Notably, the moist neutral stability layer (∼1.5–4.2 km) attains error saturation much earlier than the other levels.

The spectral results for the 1–12 km altitude range show variable- and scale-dependent intrinsic predictability of the banded convection. For the LPI threshold at 60% (hereafter the same for all variables), at the 10-km scale, *rain* exhibits the shortest predictability timescale (∼4 hr). The variables *w*, *q*, and *cloud* show intermediate predictability durations of 5–6 hr, while *u* reaches approximately 7 hr. In contrast, the variables *v*, *T*, and *P* demonstrate significantly longer predictability limits exceeding 12 hr. At the 40-km scale, only *rain* and *cloud* attain the thresholds within 8 and 12 h respectively, whereas all other variables exceed 12-hr predictability limits.

This study selects two representative altitudes, including 3 km within the moist neutral stability layer and 1.3 km within the ducting stable layer. By focusing on the localized convective bands and two distinct lower-tropospheric layers, it is shown that higher moisture content corresponds to more limited predictability at specific scales, simultaneously diminishing differences in the predictable time scales among variables. The eight studied variables become more correlated within the middle-level moist neutral stability layer under the coupling between GWs and convection, leading to more coherent predictability characteristics.

Sensitivity experiments on moisture (EXP80, EXP60, EXP40, EXP20, and the extremely dry EXP00) demonstrate that the reference power spectra of eight variables at meso- and micro-scales (e.g., <∼100 km in this case) generally show greater sensitivity to initial moisture conditions. Additionally, the sensitivity of different variables to moisture varies, with the reference power spectra of temperature and pressure showing lower sensitivity and *cloud* and *rain* exhibiting nearly uniform sensitivity across all scales. Under a dry environment, the predictability timescales of all variables are uniformly extended beyond 12 hr with very low error growth rates regardless of regional focus or vertical level selection, which gives a further demonstration that moist convection plays an essential role in organizing and amplifying small-scale small-amplitude perturbations over the early stages of the simulations (Tan et al., 2004; Zhang et al., 2003, 2007).

The horizontal kinetic energy spectrum is further decomposed into divergent and rotational components (proxies for unbalanced and balanced components, respectively), which demonstrate contrasting behaviors in the power spectrum, intrinsic predictability limit, and sensitivity to different initial moist contents. Across all sensitivity experiments, the vertically averaged divergent kinetic energy spectra exhibit much shallower slopes than the rotational kinetic energy spectra. The results show that the vertically averaged divergent kinetic energy constitutes a minority fraction across all scales above the effective resolution in the CNTL experiment. However, since the divergent component is closely linked with the gravity wave dynamics (or the unbalanced mode in general), divergent and rotational kinetic energy contributions become comparable in the ducting stable layer with horizontally propagating GWs. Furthermore, a reduction in initial moisture weakens both divergent and rotational kinetic energy at all levels, while the divergent component exhibits relatively smaller attenuation, especially in the low-level ducting stable layer, which suggests that the wave duct still exists even in dry processes. Under this condition, the LPI growth rates for both energy components also decrease.

The moist neutral stability layer exhibits a more limited intrinsic predictability of *div* and *rot* variables compared to the ducting stable layer. Despite the dominance of rotational kinetic energy, the lower predictability observed in

the moist neutral instability layer presents a seeming paradox when viewed through the lens of classical large-scale dynamics. Typically, balanced rotational flows are associated with a steep k^{-3} energy spectrum that implies limited error growth and essentially better predictability (Charney, 1971; Rotunno & Snyder, 2008). However, it is crucial to note that our study focuses on the mesoscale range (e.g., wavelengths of ~40–50 km). The rotational kinetic energy has a quasi −5/3 spectral slope within the wavelength range of 10–40 km [15–100 km in Sun et al. (2017)]. At these scales, the physical nature of the rotational component differs significantly from that of large-scale geostrophic flow. The generation of rotational kinetic energy in moist environments relies critically on the stretching of vorticity by convective updrafts. Unlike the slow-evolving synoptic waves, these convectively driven mesoscale vortices are intrinsically linked to the rapid, nonlinear evolution of moist convection and are driven by the release of latent heat. Therefore, in the specific context of the moist neutral instability layer at 40–50 km scales, the rotational dominance does not guarantee the high predictability (as well as the steep spectral slope) seen at synoptic scales. Instead, the predictability is limited using moist convective processes, which act as a catalyst for rapid error growth while sustaining these rotational features.

In addition, this study also reveals the intricate relationship between the reference power spectral slope and intrinsic predictability. It is generally expected that the shallower (i.e., flatter) the spectrum, the more energy at the smaller scales, and thus the more limited predictability for any given variable. This expectation has been verified extensively in this study, but with some noticeable exceptions. For example, several counterexamples can be found in the following cases: (a) temperature (or the corresponding available potential energy) versus horizontal wind (or the corresponding horizontal kinetic energy) (Figures S1a–S1c); (b) cloud water in EXP60 versus cloud water in EXP00 (Figure 11g); (c) rotational kinetic energy in the moist neutral stability layer versus rotational kinetic energy in the ducting stable layer (Figures 17b and 17e). In all these above counterexamples, a shallower spectral slope is associated with higher predictability. However, further verification reveals that these shallower slopes actually correspond to weaker power spectral amplitudes, and thus weaker instabilities. This may explain why error growth is slower, resulting in less limited predictability. In conclusion, error growth behaviors and intrinsic predictability limit are closely linked with the corresponding reference power spectral slope, but they are also impacted by other factors including but not limited to, power spectral amplitude, moisture content, vertical flow structure, and the selected metrics for quantification under different background flow.

It should be clarified that the current results on the variables-dependent intrinsic predictability of wave-convection coupled bands may only apply to this event. Recently, Zhou et al. (2024) identified over 110 wavelike banded convection events using historic radar mosaic maps over the same region, and they further investigated the statistical characteristics of wavelike banded convection associated with ducted GWs. In the future, more high-resolution numerical case studies will be conducted to clarify the intrinsic predictability of wave-convection coupled bands, which may vary under different atmospheric conditions. Complementary to these multi-case investigations, future research will also employ structure function analysis (Monin & Yaglom, 1975) to validate the spectral findings within physical space. The inertial range characteristic (i.e., the $k^{-5/3}$ slope) observed in the power spectra is physically robust and can even be transposed into physical space using structure functions. For instance, Orszag (1977) demonstrated that for the inertial range, the second-order structure function scales as the 2/3 power of the spatial distance (i.e., $r^{2/3}$). Furthermore, Lu and Koch (2008) utilized structure function analyses to identify localized regions of the inverse energy cascade and energy convergence between turbulence and small-scale gravity waves. By integrating these advanced physical-space diagnostics with broader statistical investigations, a more unified understanding of the dynamic mechanisms constraining mesoscale predictability will be achieved.

Conflict of Interest

The authors declare no conflicts of interest relevant to this study.

Availability Statement

The initial and lateral boundary conditions in the simulations are created by the NCEP Final Analysis (GFS-FNL) data set (National Centers for Environmental Prediction, 2000). Version 3.8.1 of the WRF model (Skamarock

et al., 2008) used for numerical simulations in this study can be accessed at https://www2.mmm.ucar.edu/wrf/users/download/get_sources.html.

Acknowledgments
This work was supported by the National Natural Science Foundation of China (42375003, 42475002 and 42075005), the Guangdong Basic and Applied Basic Research Foundation (2024A1515012470), and the Science and Technology Planning Project of Guangdong Province (2023B1212060019, 2024A1515510005, 2025A1515011974, and 2020B1212060025). This project was also supported by Southern Marine Science and Engineering Guangdong Laboratory (Zhuhai) (SML2024SP012), and the Innovation Group Project of Southern Marine Science and Engineering Guangdong Laboratory (Zhuhai) (311024001).

References

Bei, N., & Zhang, F. (2007). Impacts of initial condition errors on mesoscale predictability of heavy precipitation along the Mei-Yu front of China. *Quarterly Journal of the Royal Meteorological Society*, *133*(622), 83–99. https://doi.org/10.1002/qj.20

Bei, N., & Zhang, F. (2014). Mesoscale predictability of moist baroclinic waves: Variable and scale-dependent error growth. *Advances in Atmospheric Sciences*, *31*(5), 995–1008. https://doi.org/10.1007/s00376-014-3191-7

Bierdel, L., Selz, T., & Craig, G. C. (2018). Theoretical aspects of upscale error growth on the mesoscales: Idealized numerical simulations. *Quarterly Journal of the Royal Meteorological Society*, *144*(712), 682–694. https://doi.org/10.1002/qj.3236

Bierdel, L., Snyder, C., Park, S. H., & Skamarock, W. C. (2016). Accuracy of rotational and divergent kinetic energy spectra diagnosed from flight-track winds. *Journal of the Atmospheric Sciences*, *73*(8), 3273–3286. https://doi.org/10.1175/JAS-D-16-0040.1

Blažica, V., Žagar, N., Strajnar, B., & Cedilnik, J. (2013). Rotational and divergent kinetic energy in the mesoscale model ALADIN. *Tellus, Series A: Dynamic Meteorology and Oceanography*, *65*(1), 18918. https://doi.org/10.3402/tellusa.v65i0.18918

Bosart, L. F., Bracken, W. E., & Seimon, A. (1998). A study of cyclone mesoscale structure with emphasis on a large-amplitude inertia-gravity wave. *Monthly Weather Review*, *126*(6), 1497–1527. https://doi.org/10.1175/1520-0493(1998)126<1497:ASOCMS>2.0.CO;2

Bretherton, C. (1988). Group velocity and the linear response of stratified fluids to internal heat or mass sources. *Journal of the Atmospheric Sciences*, *45*(1), 81–94. https://doi.org/10.1175/1520-0469(1988)045<0081:GVATLR>2.0.CO;2

Callies, J., Ferrari, R., & Bühler, O. (2014). Transition from geostrophic turbulence to inertia-gravity waves in the atmospheric energy spectrum. *Proceedings of the National Academy of Sciences of the United States of America*, *111*(48), 17033–17038. https://doi.org/10.1073/pnas.1410772111

Charney, J. G. (1971). Geostrophic turbulence. *Journal of the Atmospheric Sciences*, *28*(6), 1087–1095. https://doi.org/10.1175/1520-0469(1971)028<1087:gt>2.0.co;2

Charney, J. G., Fleagle, R. G., Riehl, H., Lally, V. E., & Wark, D. Q. (1966). The feasibility of a global observation and analysis experiment. *Bulletin of the American Meteorological Society*, *47*, 200–220.

Chasteen, M. B., & Koch, S. E. (2022). Multiscale aspects of the 26–27 April 2011 tornado outbreak. Part II: Environmental modifications and upscale feedbacks arising from latent processes. *Monthly Weather Review*, *150*(2), 337–368. https://doi.org/10.1175/MWR-D-21-0014.1

Clarke, R. H. (1972). The morning glory: An atmospheric hydraulic jump. *Journal of Applied Meteorology*, *11*(2), 304–311. https://doi.org/10.1175/1520-0450(1972)011<0304:TMGAAH>2.0.CO;2

Denis, B., Côté, J., & Laprise, R. (2002). Spectral decomposition of two-dimensional atmospheric fields on limited-area domains using the discrete cosine transform (DCT). *Monthly Weather Review*, *130*(7), 1812–1829. https://doi.org/10.1175/1520-0493(2002)130<1812:SDOTDA>2.0.CO;2

Dewan, E. (1997). Saturated-cascade similitude theory of gravity wave spectra. *Journal of Geophysical Research*, *102*(D25), 29799–29817. https://doi.org/10.1029/97JD02151

Dewan, E. M. (1979). Stratospheric wave spectra resembling turbulence. *Science*, *204*(4395), 832–835. https://doi.org/10.1126/science.204.4395.832

Du, Y., Rotunno, R., Chen, Z., & Yang, H. (2024). A linear theory for periodic convectively forced gravity waves near a coastline. *Journal of the Atmospheric Sciences*, *81*(7), 1271–1288. https://doi.org/10.1175/JAS-D-23-0173.1

Du, Y., & Zhang, F. (2019). Banded convective activity associated with mesoscale gravity waves over southern China. *Journal of Geophysical Research: Atmospheres*, *124*(4), 1912–1930. https://doi.org/10.1029/2018JD029523

Du, Y., Zhang, F., Sun, Y. Q., Wei, J., & Li, X. (2021). Practical and intrinsic predictability of wave-convection coupled bands over southern China. *Journal of Geophysical Research: Atmospheres*, *126*(22), e2021JD034882. https://doi.org/10.1029/2021JD034882

Ehrendorfer, M., Errico, R. M., & Raeder, K. D. (1999). Singular-vector perturbation growth in a primitive equation model with moist physics. *Journal of the Atmospheric Sciences*, *56*(11), 1627–1648. https://doi.org/10.1175/1520-0469(1999)056<1627:SVPGIA>2.0.CO;2

Errico, R., & Baumhefner, D. (1987). Predictability experiments using a high-resolution limited-area model. *Monthly Weather Review*, *115*(2), 488–504. https://doi.org/10.1175/1520-0493(1987)115<0488:PEUAHR>2.0.CO;2

Errico, R. M. (1985). Spectra computed from a limited area grid. *Monthly Weather Review*, *113*(9), 1554–1562. https://doi.org/10.1175/1520-0493(1985)113<1554:SCFALA>2.0.CO;2

Fovell, R., Durran, D., & Holton, J. R. (1992). Numerical simulations of convectively generated stratospheric gravity waves. *Journal of the Atmospheric Sciences*, *49*(16), 1427–1442. https://doi.org/10.1175/1520-0469(1992)049<1427:NSOCGS>2.0.CO;2

Hamilton, K., Takahashi, Y. O., & Ohfuchi, W. (2008). Mesoscale spectrum of atmospheric motions investigated in a very fine resolution global general circulation model. *Journal of Geophysical Research*, *113*(D18), D18110. https://doi.org/10.1029/2008JD009785

Hong, S. Y., Noh, Y., & Dudhia, J. (2006). A new vertical diffusion package with an explicit treatment of entrainment processes. *Monthly Weather Review*, *134*(9), 2318–2341. https://doi.org/10.1175/MWR3199.1

Iacono, M. J., Delamere, J. S., Mlawer, E. J., Shephard, M. W., Clough, S. A., & Collins, W. D. (2008). Radiative forcing by long-lived greenhouse gases: Calculations with the AER radiative transfer models. *Journal of Geophysical Research*, *113*(13), D13103. https://doi.org/10.1029/2008JD009944

Jiménez, P. A., Dudhia, J., González-Rouco, J. F., Navarro, J., Montávez, J. P., & García-Bustamante, E. (2012). A revised scheme for the WRF surface layer formulation. *Monthly Weather Review*, *140*(3), 898–918. https://doi.org/10.1175/MWR-D-11-00056.1

Judt, F. (2018). Insights into atmospheric predictability through global convection-permitting model simulations. *Journal of the Atmospheric Sciences*, *75*(5), 1477–1497. https://doi.org/10.1175/JAS-D-17-0343.1

Judt, F. (2020). Atmospheric predictability of the tropics, middle latitudes, and polar regions explored through global storm-resolving simulations. *Journal of the Atmospheric Sciences*, *77*(1), 257–276. https://doi.org/10.1175/JAS-D-19-0116.1

Kain, J. S. (2004). The Kain - Fritsch convective parameterization: An update. *Journal of Applied Meteorology*, *43*(1), 170–181. https://doi.org/10.1175/1520-0450(2004)043<0170:TKCPAU>2.0.CO;2

Knobloch, S., Kaifler, B., Dörnbrack, A., & Rapp, M. (2023). Horizontal wavenumber spectra across the middle atmosphere from airborne LiDAR observations during the 2019 southern hemispheric SSW. *Geophysical Research Letters*, *50*(14), e2023GL104357. https://doi.org/10.1029/2023GL104357

Koch, S. E., Golus, R. E., & Dorian, P. B. (1988). A mesoscale gravity wave event observed during CCOPE. Part II: Interactions between mesoscale convective systems and the antecedent waves. *Monthly Weather Review*, *116*(12), 2545–2569. https://doi.org/10.1175/1520-0493(1988)116<2545:AMGWEO>2.0.CO;2

Kolmogorov, A. N. (1941). The local structure of turbulence in incompressible viscous fluid for very large Reynolds number. *Doklady Akademii Nauk SSSR*, *30*, 301–305.

Koppel, L. L., Bosart, L. F., & Keyser, D. (2000). A 25-yr climatology of large-amplitude hourly surface pressure changes over the conterminous United States. *Monthly Weather Review*, *128*(1), 51–68. https://doi.org/10.1175/1520-0493(2000)128<0051:AYCOLA>2.0.CO;2

Kouhen, S., Storer, B. A., Aluie, H., Marshall, D. P., & Christensen, H. M. (2024). Convective and orographic origins of the mesoscale kinetic energy spectrum. *Geophysical Research Letters*, *51*(21), e2024GL110804. https://doi.org/10.1029/2024GL110804

Kraichnan, R. H. (1967). Inertial ranges in two-dimensional turbulence. *Physics of Fluids*, *10*(7), 1417–1423. https://doi.org/10.1063/1.1762301

Lane, T. P., Reeder, M. J., & Clark, T. L. (2001). Numerical modeling of gravity wave generation by deep tropical convection. *Journal of the Atmospheric Sciences*, *58*(10), 1249–1274. https://doi.org/10.1175/1520-0469(2001)058<1249:NMOGWG>2.0.CO;2

Lane, T. P., & Zhang, F. (2011). Coupling between gravity waves and tropical convection at mesoscales. *Journal of the Atmospheric Sciences*, *68*(11), 2582–2598. https://doi.org/10.1175/2011JAS3577.1

Leith, C. E., & Kraichnan, R. H. (1972). Predictability of turbulent flows. *Journal of the Atmospheric Sciences*, *29*(6), 1041–1058. https://doi.org/10.1175/1520-0469(1972)029<1041:POTF>2.0.CO;2

Li, L., & Chen, Y. L. (2017). Numerical simulations of two trapped mountain lee waves downstream of Oahu. *Journal of Applied Meteorology and Climatology*, *56*(5), 1305–1324. https://doi.org/10.1175/JAMC-D-15-0341.1

Li, Z., Wei, J., Bao, X., & Sun, Y. Q. (2023). Intercomparison of tropospheric and stratospheric mesoscale kinetic energy resolved by the high-resolution global reanalysis datasets. *Quarterly Journal of the Royal Meteorological Society*, *149*(757), 3738–3764. https://doi.org/10.1002/qj.4605

Lin, Y.-L., & Chun, H.-Y. (1991). Effects of diabatic cooling in a shear flow with a critical level. *Journal of the Atmospheric Sciences*, *48*(23), 2476–2491. https://doi.org/10.1175/1520-0469(1991)048<2476:EODCIA>2.0.CO;2

Lindborg, E. (1999). Can the atmospheric kinetic energy spectrum be explained by two-dimensional turbulence? *Journal of Fluid Mechanics*, *388*, 259–288. https://doi.org/10.1017/S0022112099004851

Lindzen, R. S. (1974). Wave-CISK in the tropics. *Journal of the Atmospheric Sciences*, *31*(1), 156–179. https://doi.org/10.1175/1520-0469(1974)031<0156:WCITT>2.0.CO;2

Lindzen, R. S., & Tung, K.-K. (1976). Banded convective activity and ducted gravity waves. *Monthly Weather Review*, *104*(12), 1602–1617. https://doi.org/10.1175/1520-0493(1976)104<1602:BCAADG>2.0.CO;2

Livneh, B., Restrepo, P. J., & Lettenmaier, D. P. (2011). Development of a unified land model for prediction of surface hydrology and land-atmosphere interactions. *Journal of Hydrometeorology*, *12*(6), 1299–1320. https://doi.org/10.1175/2011JHM1361.1

Lloveras, D. J., Tierney, L. H., & Durran, D. R. (2022). Mesoscale predictability in moist midlatitude cyclones is not sensitive to the slope of the background kinetic energy spectrum. *Journal of the Atmospheric Sciences*, *79*(1), 119–139. https://doi.org/10.1175/JAS-D-21-0147.1

Lorenz, E. N. (1969). The predictability of a flow which possesses many scales of motion. *Tellus*, *21*(3), 289–307. https://doi.org/10.3402/tellusa.v21i3.10086

Lorenz, E. N. (1982). Atmospheric predictability experiments with a large numerical model. *Tellus*, *34*(6), 505–513. https://doi.org/10.3402/tellusa.v34i6.10836

Lorenz, E. N. (1996). Predictability—A problem partly solved. In *Proceedings of seminar on predictability* (pp. 1–18). ECMWF.

Lu, C., & Koch, S. E. (2008). Interaction of upper-tropospheric turbulence and gravity waves as obtained from spectral and structure function analyses. *Journal of the Atmospheric Sciences*, *65*(8), 2676–2690. https://doi.org/10.1175/2007JAS2660.1

Melhauser, C., & Zhang, F. (2012). Practical and intrinsic predictability of severe and convective weather at the mesoscales. *Journal of the Atmospheric Sciences*, *69*(11), 3350–3371. https://doi.org/10.1175/JAS-D-11-0315.1

Métais, O., & Lesieur, M. (1986). Statistical predictability of decaying turbulence. *Journal of the Atmospheric Sciences*, *43*(9), 857–870. https://doi.org/10.1175/1520-0469(1986)043<0857:SPODT>2.0.CO;2

Min, J., & Wu, N. (2020). Advances in atmospheric predictability of heavy rain and severe convection (in Chinese). *Chinese Journal of Atmospheric Sciences*, *44*(5), 1039–1056. https://doi.org/10.3878/j.issn.1006-9895.2003.19186

Monin, A. S., & Yaglom, A. M. (1975). *Statistical fluid mechanics: Mechanics of turbulence* (Vol. 2). MIT Press.

Morss, R. E., Snyder, C., & Rotunno, R. (2009). Spectra, spatial scales, and predictability in a quasigeostrophic model. *Journal of the Atmospheric Sciences*, *66*(10), 3115–3130. https://doi.org/10.1175/2009JAS3057.1

Mu, M., Duan, W. S., & Tang, Y. M. (2017). The predictability of atmospheric and oceanic motions: Retrospect and prospects. *Science China Earth Sciences*, *60*(11), 2001–2012. https://doi.org/10.1007/s11430-016-9101-x

Nastrom, G. D., & Gage, K. S. (1985). A climatology of atmospheric wavenumber spectra of wind and temperature observed by commercial aircraft. *Journal of the Atmospheric Sciences*, *42*(9), 950–960. https://doi.org/10.1175/1520-0469(1985)042<0950:ACOAWS>2.0.CO;2

Nastrom, G. D., Gage, K. S., & Jasperson, W. H. (1984). Kinetic energy spectrum of large-and mesoscale atmospheric processes. *Nature*, *310*(5972), 36–38. https://doi.org/10.1038/310036a0

National Centers for Environmental Prediction (NCEP). (2000). NCEP FNL Operational Model Global Tropospheric Analyses, continuing from July 1999 [Dataset]. *NSF National Center for Atmospheric Research*. https://doi.org/10.5065/D6M043C6

Orszag, S. A. (1977). Lectures on the statistical theory of turbulence. In R. Balian & J. L. Peube (Eds.), *Fluid dynamics* (pp. 237–374). Gordon & Breach.

Peng, J., Zhang, L., Luo, Y., & Zhang, Y. (2014). Mesoscale energy spectra of the Mei-Yu front system. Part I: Kinetic energy spectra. *Journal of the Atmospheric Sciences*, *71*(1), 37–55. https://doi.org/10.1175/JAS-D-13-085.1

Powers, J. G., & Reed, R. J. (1993). Numerical simulation of the large-amplitude mesoscale gravity-wave event of 15 December 1987 in the central United States. *Monthly Weather Review*, *121*(8), 2285–2308. https://doi.org/10.1175/1520-0493(1993)121<2285:NSOTLA>2.0.CO;2

Queney, P. (1948). The problem of air flow over mountains: A summary of theoretical studies. *Bulletin of the American Meteorological Society*, *29*(1), 16–26. https://doi.org/10.1175/1520-0477-29.1.16

Raymond, D. J. (1975). A model for predicting the movement of continuously propagating convective storms. *Journal of the Atmospheric Sciences*, *32*(7), 1308–1317. https://doi.org/10.1175/1520-0469(1975)032<1308:AMFPTM>2.0.CO;2

Reynolds, C. A., Webster, P. J., & Kalnay, E. (1994). Random error growth in NMC's global forecasts. *Monthly Weather Review*, *122*(6), 1281–1305. https://doi.org/10.1175/1520-0493(1994)122<1281:REGING>2.0.CO;2

Rotunno, R., & Snyder, C. (2008). A generalization of Lorenz's model for the predictability of flows with many scales of motion. *Journal of the Atmospheric Sciences*, *65*(3), 1063–1076. https://doi.org/10.1175/2007JAS2449.1

Rotunno, R., Snyder, C., & Judt, F. (2023). Upscale versus "up-amplitude" growth of forecast-error spectra. *Journal of the Atmospheric Sciences*, *80*(1), 63–72. https://doi.org/10.1175/JAS-D-22-0070.1

Ruppert, J. H., Koch, S. E., Chen, X., Du, Y., Seimon, A., Sun, Y. Q., et al. (2024). Mesoscale gravity waves & midlatitude weather: The inspiring determination and dedication of Fuqing Zhang. *Bulletin of the American Meteorological Society*, *103*(9), 680–683. https://doi.org/10.1175/BAMS-D-20-0005.A

Ruppert, J. H., Koch, S. E., Chen, X., Du, Y., Seimon, A., Sun, Y. Q., et al. (2022). Mesoscale gravity waves and midlatitude weather: A tribute to Fuqing Zhang. *Bulletin of the American Meteorological Society*, *103*(1), E129–E156. https://doi.org/10.1175/BAMS-D-20-0005.1

Selz, T. (2019). Estimating the intrinsic limit of predictability using a stochastic convection scheme. *Journal of the Atmospheric Sciences*, *76*(3), 757–765. https://doi.org/10.1175/JAS-D-17-0373.1

Skamarock, W. C. (2004). Evaluating mesoscale NWP models using kinetic energy spectra. *Monthly Weather Review*, *132*(12), 3019–3032. https://doi.org/10.1175/MWR2830.1

Skamarock, W. C., Klemp, J. B., Dudhia, J., Gill, D. O., Barker, D., Duda, M. G., et al. (2008). A description of the advanced research WRF version 3 [Software]. *NCAR Tech. Note NCAR/TN-475+STR*, 113. https://doi.org/10.5065/D68S4MVH

Skamarock, W. C., Park, S. H., Klemp, J. B., & Snyder, C. (2014). Atmospheric kinetic energy spectra from global high-resolution nonhydrostatic simulations. *Journal of the Atmospheric Sciences*, *71*(11), 4369–4381. https://doi.org/10.1175/JAS-D-14-0114.1

Smith, R. B. (1980). Linear theory of stratified hydrostatic flow past an isolated mountain. *Tellus*, *32*(4), 348–364. https://doi.org/10.1111/j.2153-3490.1980.tb00962.x

Snyder, C., Hamill, T. M., & Trier, S. B. (2003). Linear evolution of error covariances in a quasigeostrophic model. *Monthly Weather Review*, *131*(1), 189–205. https://doi.org/10.1175/1520-0493(2003)131<0189:LEOECI>2.0.CO;2

Stephan, C. C., Duras, J., Harris, L., Klocke, D., Putman, W. M., Taylor, M., et al. (2022). Atmospheric energy spectra in global kilometre-scale models. *Tellus, Series A: Dynamic Meteorology and Oceanography*, *74*(1), 280–299. https://doi.org/10.16993/tellusa.26

Sun, Y. Q., Rotunno, R., & Zhang, F. (2017). Contributions of moist convection and internal gravity waves to building the atmospheric -5/3 kinetic energy spectra. *Journal of the Atmospheric Sciences*, *74*(1), 185–201. https://doi.org/10.1175/JAS-D-16-0097.1

Sun, Y. Q., & Zhang, F. (2016). Intrinsic versus practical limits of atmospheric predictability and the significance of the butterfly effect. *Journal of the Atmospheric Sciences*, *73*(3), 1419–1438. https://doi.org/10.1175/JAS-D-15-0142.1

Tan, Z. M., Zhang, F., Rotunno, R., & Snyder, C. (2004). Mesoscale predictability of moist baroclinic waves: Experiments with parameterized convection. *Journal of the Atmospheric Sciences*, *61*(14), 1794–1804. https://doi.org/10.1175/1520-0469(2004)061<1794:MPOMBW>2.0.CO;2

Thompson, G., Field, P. R., Rasmussen, R. M., & Hall, W. D. (2008). Explicit forecasts of winter precipitation using an improved bulk microphysics scheme. Part II: Implementation of a new snow parameterization. *Monthly Weather Review*, *136*(12), 5095–5115. https://doi.org/10.1175/2008MWR2387.1

Uccellini, L. W., & Koch, S. E. (1987). The synoptic setting and possible energy sources for mesoscale wave disturbances. *Monthly Weather Review*, *115*(3), 721–729. https://doi.org/10.1175/1520-0493(1987)115<0721:TSSAPE>2.0.CO;2

Waite, M. L., & Snyder, C. (2013). Mesoscale energy spectra of moist baroclinic waves. *Journal of the Atmospheric Sciences*, *70*(4), 1242–1256. https://doi.org/10.1175/JAS-D-11-0347.1

Wang, Y., Zhang, L., Peng, J., & Liu, S. (2018). Mesoscale horizontal kinetic energy spectra of a tropical cyclone. *Journal of the Atmospheric Sciences*, *75*(10), 3579–3596. https://doi.org/10.1175/JAS-D-17-0391.1

Wei, J. (2026). Gravity waves | Convectively generated gravity waves. In W. A. Robinson (Ed.), *Encyclopedia of atmospheric sciences* (Vol. 4, pp. 171–189). Elsevier, Academic Press. https://doi.org/10.1016/B978-0-323-96026-7.00215-0

Wei, J., & Zhang, F. (2014). Mesoscale gravity waves in moist baroclinic jet-front systems. *Journal of the Atmospheric Sciences*, *71*(3), 929–952. https://doi.org/10.1175/JAS-D-13-0171.1

Wei, J., & Zhang, F. (2015). Tracking gravity waves in moist baroclinic jet-front systems. *Journal of Advances in Modeling Earth Systems*, *7*(1), 67–91. https://doi.org/10.1002/2014MS000395

Wei, J., Zhang, F., & Richter, J. H. (2016). An analysis of gravity wave spectral characteristics in moist baroclinic jet-front systems. *Journal of the Atmospheric Sciences*, *73*(8), 3133–3155. https://doi.org/10.1175/JAS-D-15-0316.1

Wirth, A., & Ghil, M. (2000). Error evolution in the dynamics of an ocean general circulation model. *Dynamics of Atmospheres and Oceans*, *32*(3–4), 419–431. https://doi.org/10.1016/S0377-0265(00)00053-1

Yang, H., & Du, Y. (2024). Difference between upshear- and downshear-propagating waves associated with the development of squall lines. *Monthly Weather Review*, *152*(6), 1399–1420. https://doi.org/10.1175/MWR-D-23-0109.1

Yang, H., & Du, Y. (2026). Distinct convection initiation near and far ahead of an idealized squall line. *Journal of the Atmospheric Sciences*, *83*(1), 151–168. https://doi.org/10.1175/JAS-D-25-0073.1

Yang, H., Du, Y., Chen, Z., & Gao, X. (2026). Convection initiation over mountain slopes in North China: Roles of upslope winds and orographic waves. *Advances in Atmospheric Sciences*, *43*(5), 889–906. https://doi.org/10.1007/s00376-025-5589-9

Yang, S.-N. (2011). *A study on mesoscale predictability of Meiyu heavy rainfall over the Yangtze-Huaihe basin (in Chinese)* (Doctoral dissertation). Nanjing University.

Ying, Y., & Zhang, F. (2017). Practical and intrinsic predictability of multiscale weather and convectively coupled equatorial waves during the active phase of an MJO. *Journal of the Atmospheric Sciences*, *74*(11), 3771–3785. https://doi.org/10.1175/JAS-D-17-0157.1

Žagar, N., Horvat, M., Zaplotnik, Ž., & Magnusson, L. (2017). Scale-dependent estimates of the growth of forecast uncertainties in a global prediction system. *Tellus, Series A: Dynamic Meteorology and Oceanography*, *69*(1), 1287492. https://doi.org/10.1080/16000870.2017.1287492

Žagar, N., Jelić, D., Blaauw, M., & Bechtold, P. (2017). Energy spectra and inertia-gravity waves in global analyses. *Journal of the Atmospheric Sciences*, *74*(8), 2447–2466. https://doi.org/10.1175/JAS-D-16-0341.1

Zhang, F. (2004). Generation of mesoscale gravity waves in upper-tropospheric jet-front systems. *Journal of the Atmospheric Sciences*, *61*(4), 440–457. https://doi.org/10.1175/1520-0469(2004)061<0440:GOMGWI>2.0.CO;2

Zhang, F., Bei, N., Rotunno, R., Snyder, C., & Epifanio, C. C. (2007). Mesoscale predictability of moist baroclinic waves: Convection-permitting experiments and multistage error growth dynamics. *Journal of the Atmospheric Sciences*, *64*(10), 3579–3594. https://doi.org/10.1175/JAS4028.1

Zhang, F., Davis, C. A., Kaplan, M. L., & Koch, S. E. (2001). Wavelet analysis and the governing dynamics of a large-amplitude mesoscale gravity-wave event along the East Coast of the United States. *Quarterly Journal of the Royal Meteorological Society*, *127*(577), 2209–2245. https://doi.org/10.1002/qj.49712757702

Zhang, F., Odins, A. M., & Nielsen-Gammon, J. W. (2006). Mesoscale predictability of an extreme warm-season precipitation event. *Weather and Forecasting*, *21*(2), 149–166. https://doi.org/10.1175/WAF909.1

Zhang, F., Qiang Sun, Y., Magnusson, L., Buizza, R., Lin, S. J., Chen, J. H., & Emanuel, K. (2019). What is the predictability limit of midlatitude weather? *Journal of the Atmospheric Sciences*, *76*(4), 1077–1091. https://doi.org/10.1175/JAS-D-18-0269.1

Zhang, F., Snyder, C., & Rotunno, R. (2003). Effects of moist convection on mesoscale predictability. *Journal of the Atmospheric Sciences*, *60*(9), 1173–1185. https://doi.org/10.1175/1520-0469(2003)060<1173:EOMcom>2.0.CO;2

Zhang, F., Wei, J., Zhang, M., Bowman, K. P., Pan, L. L., Atlas, E., & Wofsy, S. C. (2015). Aircraft measurements of gravity waves in the upper troposphere and lower stratosphere during the START08 field experiment. *Atmospheric Chemistry and Physics*, *15*(13), 7667–7684. https://doi.org/10.5194/acp-15-7667-2015

Zhang, W., Peng, J., Zhang, W., Li, Z., & Wu, H. (2024). The rotational and divergent kinetic energy spectra of geostrophic vortices and inertia-gravity waves. *Journal of Geophysical Research: Atmospheres*, *129*(7), e2023JD040542. https://doi.org/10.1029/2023JD040542

Zhou, X., Du, Y., Wei, J., Chen, Z., & Yang, H. (2024). Statistical characteristics of wavelike banded convection associated with ducted gravity waves over southern China. *Geophysical Research Letters*, *51*(20), e2024GL112027. https://doi.org/10.1029/2024GL112027